

On modeling fracture of soft polymers

Aditya Konale^a, Vikas Srivastava^{a,b,*}

^a*School of Engineering, Brown University, Providence, RI 02912, USA*

^b*Institute for Biology, Engineering and Medicine, Brown University, Providence, RI 02912, USA*

Abstract

Soft polymers are ubiquitous materials found in nature and as engineering materials with properties varying from rate-independent to significantly rate-dependent depending on the crosslinking mechanisms. Current fracture toughness measures such as energy release rate are non-unique for rate-dependent soft materials for varying loading profiles and specimen geometries. Works on modeling fracture in rate-dependent soft polymers are limited to crack tip stress field analyses or crack tip driving force approaches for specific pre-cracked geometries. We have developed a model to predict damage initiation and growth in soft polymers based on a generalized multi-mechanism gradient damage framework. We propose and show that a critical value of stress work W_{cr} can uniquely quantify the total energy dissipation per unit referential volume associated with the complete failure of a material point under a loading mode. W_{cr} can be evaluated using homogeneous deformation experiments and without a constitutive model. W_{cr} is demonstrated to be approximately constant with strain rate for two rate-dependent soft polymers and different loading modes for an elastomer. We propose the energetic contribution to W_{cr} as a suitable damage initiation criterion. The proposed initiation criterion in the damage model enabled successful predictions of fracture in an important rate-stiffening soft polymer Polyborosiloxane in a variety of experiments involving different specimen geometries and loading conditions. The model also provides a consistent energy density estimate for fracture-associated microstructural processes in Polyborosiloxane. The broader applicability of the fracture model is shown by its ability to predict fracture in an elastomer (EPDM) and another viscous soft polymer (EPS25 vitrimer).

Keywords: Soft polymers; Gradient damage; Fracture; Rate-dependent; Constitutive model

*Corresponding author

Email address: vikas_srivastava@brown.edu (Vikas Srivastava)

1. Introduction

Soft polymers are defined as a broad class of polymers with chain networks formed through permanent or dynamic chemical or mechanical crosslinks leading to elastic modulus in the range of a few kilopascals to tens of megapascals. This class encompasses elastomers, viscoelastic and elastic-viscoplastic polymers, polymer gels¹, and biological tissues. Their physical forms can vary from very viscous slowly flowing soft solids (Konale et al., 2023) to elastomeric rubber-like materials (Steck et al., 2019).

Such polymers form a key class of engineering materials with a broad range of applications varying from biomedical drug delivery (Shukla et al., 2020, Huebsch et al., 2014) and health monitoring (Amjadi et al., 2015, Miranda et al., 2022) to impact protection (Zong et al., 2021, Tang et al., 2022), actuation (Yuk et al., 2017, Narumi et al., 2019), and adhesives (Yuk et al., 2016, 2019). These polymers possess significant variations in mechanical properties due to their underlying crosslinking mechanisms. Permanent crosslinks result in rate-independent behavior with high elasticity like elastomers (Nunes, 2011, Steck et al., 2019). On the other hand, dynamic, reversible crosslinks lead to significantly rate-dependent mechanical behavior. (Hu et al., 2017, Kurkin et al., 2021). In the case of dynamically crosslinked polymers, longer loading timescales lead to highly viscous fluid-like behavior, while shorter loading timescales result in elastomer-like behavior. (Konale et al., 2023, Lai et al., 2019). The dynamic crosslinks can provide autonomous self-healing of small fractures (Lai et al., 2019). Hence, depending on the nature of crosslinks in a soft polymer, its behavior can vary between the extremes of *purely elastic to highly viscous response*. Current fracture toughness measures based on energy release rate or crack tip stress intensity are non-unique when evaluated for rate-dependent soft materials. They vary with the loading profile and specimen geometry under consideration (Song et al., 2021, Long and Hui, 2016, Long et al., 2021, Yin et al., 2021). Material points around stress concentrators like a notch experience multi-axial non-homogeneous strain rate and stress states. Therefore, the evaluation of energy release rate or crack tip stress field-based measures will require a three-dimensional constitutive model that captures the nonlinear, rate-dependent mechanical response.

Accurate energy or field calculations for these fracture toughness measures necessitate the use of precise computational methods like the finite element method (Long and Hui, 2016, Liu et al., 2019b, Shen et al., 2021) due to the complexities of the non-linear large strain material response, geometries and boundary conditions Fakhouri et al. (2015), Jiang et al. (2019), Duncan et al. (2020), Montanari et al. (2023). Significant experimental studies

¹The polymer gels here are restricted to those where loading timescales are significantly faster than the solvent diffusion timescale.

have focused on the fracture of elastomers (Lake et al., 1967, Lake, 1995, Chen et al., 2017, Creton, 2017, Long et al., 2021). Recent modeling efforts for elastomers based on the gradient damage framework can be broadly separated into two approaches. One considers the free energy density function and driving force for damage initiation and evolution as entirely entropic following the ideal chain assumption (Miehe and Schänzel, 2014, Raina and Miehe, 2016, Gültekin et al., 2016, Wu et al., 2016). Other incorporates an energetic contribution to the free energy density function due to backbone bond or crosslink stretching (whichever is weaker) along with the conventional entropic part (Mao et al., 2017, Talamini et al., 2018, Mao and Anand, 2018a,b). Both approaches for elastomers have been shown to yield similar results for the global response, i.e., extension force vs displacement curve till rupture of specimens (Lee et al., 2023).

Rate-dependent and dynamic failures in various polymers have been experimentally studied (Rosakis and Ravichandran, 2000, Shukla et al., 2010, Mac Donald and Ravichandran, 2020, LeBlanc et al., 2020, 2018, Srivastava et al., 2000, 2002, Zheng et al., 2022, Malhotra et al., 2021, Brown et al., 2002, Malito et al., 2019, Burla et al., 2020, Liu et al., 2023). The rate-dependent fracture of soft polymers with dynamic crosslinks has been experimentally studied (Luo et al., 2014, Liu et al., 2019b, Song et al., 2021, Zhao et al., 2022, Chen and Ravi-Chandar, 2023). Mayumi and co-workers (Mayumi et al., 2016) conducted notched tension tests on Polyvinyl alcohol gels and noticed a significant decrease in failure stretch with increasing loading rates. Shen and co-workers (Shen et al., 2021) performed notched pure shear tests on EPS25 vitrimer with multi-step loading profiles. The authors observed loading rate-dependent flow-fracture (crack blunting-advancing) transitions. Qi and co-workers (Qi et al., 2024) presented a method to map the dissipation field during crack propagation in viscous soft polymers and enable individual evaluation of the intrinsic and dissipative components of fracture toughness. A nonlinear constitutive model was used by the authors to evaluate the stress field and, hence, the total energy density supplied through mechanical work at each material point. The dissipation field was then obtained by subtracting the free energy density field evaluated using the constitutive model from the total energy density field.

Modeling of the rate-dependent fracture in dynamically crosslinked soft polymers and viscous polymers is in its infancy and has been limited to crack tip stress field analyses (Guo et al., 2018, 2019, Hui et al., 2019, Liu et al., 2019b) or crack tip driving force based approach (Shen and Vernerey, 2020, Shen et al., 2021) for specific pre-cracked geometries. The crack tip stress field asymptotic analyses use the deformation and stress fields near the crack tip to predict fracture. The crack tip driving force approach relates crack propagation velocity to the energy release rate. Models with the ability to predict crack nucleation, propagation,

and coalescence in arbitrary, complex geometries are lacking and are necessary for solving a general class of problems. The gradient damage approach used for modeling mechanical damage and complete failure in a broad range of materials is a suitable choice for this purpose (Miehe et al., 2010b, Narayan and Anand, 2019, 2021, Konica and Sain, 2021, Yang et al., 2024, Hu et al., 2020).

Critical gaps in modeling and predicting damage initiation, growth, and fracture of soft polymers are (i) the establishment of a unique physical parameter to quantify fracture resistance of soft polymers, and (ii) the development of a model to predict damage initiation and growth using the gradient damage approach which is generally applicable and independent of loading history and specimen geometry.

For rate-dependent soft polymers, we considered Polyborosiloxane (PBS). PBS is a dynamically crosslinked, rate-stiffening soft polymer which is highly viscous at long timescales with a significantly rate-dependent mechanical response (Li et al., 2014, Tang et al., 2016, Zhao et al., 2021, 2020a, Kim et al., 2022). PBS flows under its weight in long timescales (minutes) and exhibits a rubber-like response with a significant shape recovery upon deformation when subjected to high loading rates. The rate-dependent fracture response of PBS has not been experimentally studied and corresponding models have not been developed, which are critical given viscous polymers such as PBS’s broad applications which include self-healing sensing and actuation (Narumi et al., 2019, Wang et al., 2018, Liu et al., 2019a) and flexible impact mitigation (Tu et al., 2023, Myronidis et al., 2022).

We have presented the following contributions in the paper: (i) proposed and show that a critical value of stress work W_{cr} can uniquely quantify the total energy dissipation per unit volume for the complete failure of a material point under a loading mode when it is subjected to loading rates sufficient to cause damage initiation. Complete failure refers to the inability to support any mechanical stress. W_{cr} can be evaluated using simple experiments involving homogeneous deformation and without a need for constitutive models, (ii) developed a model to predict damage initiation, damage growth, and complete failure in soft polymers using a multi-mechanism generalized gradient damage framework. A criterion for damage initiation ψ_{cr}^+ (the energetic contribution to W_{cr}) in the model can be evaluated using a one-dimensional numerical implementation of deformation-only constitutive model and homogeneous deformation experiment (e.g., simple tension test) results, and (iii) validated the predictive capabilities of the fracture model for an elastomer (EPDM), a viscous soft polymer (EPS25 vitrimer), and PBS.

2. Fracture in soft polymers

Notches and cracks in soft polymers undergo a significant amount of blunting before fracture initiation (Miehe and Schänzel, 2014, Luo et al., 2014). Hence, geometric non-linearity due to the large deformation corresponding to blunting has to be accounted for along with material non-linearity. Figure 1 depicts key observations during the deformation and fracture of PBS. To fabricate PBS, hydroxy-terminated Polydimethylsiloxane (PDMS, Sigma Aldrich 481963, 750 cSt) and Boric Acid (BA, Sigma Aldrich B0394, ACS reagent, $\geq 99.5\%$) were mixed in the ratio 160:1 by weight. The mixture was stirred and then heated at 120°C for 72 hrs to obtain PBS (Konale et al., 2023). A notched PBS specimen in Figure 1(a) was stretched at slow (6 mm/s) and fast (60 mm/s) rates. All tension tests on PBS in this work were conducted using the UniVert Mechanical Test System (CellScale) and at 23°C . Three replicates were performed for each experimental result reported. We applied 3D-printed Polylactic acid (PLA) custom fixtures to avoid creeping of PBS under the clamping pressure of conventional spring-loaded grips. In the custom fixtures shown in Figure 1(a), parts of the specimen outside the gauge length are glued to the fixture’s interior faces using a cyanoacrylate adhesive. PBS’s rate-dependent fracture response is highlighted in Figure 1(b) through a transition from high extensibility at a slow deformation rate without fracture to fracture with low extensibility at a fast loading rate. Figure 1(c) shows the specimen geometry evolution with stretching load through damage evolution and complete failure at the 60 mm/s loading rate. The high extent of notch blunting before notch propagation can be observed in Figure 1(c). The presence of viscous effects in soft polymers results in a trumpet-like fracture profile (formation of second local notch ahead of the original blunted notch) (de Gennes, 1996, Hui et al., 2022). Figure 1(d) shows deformation profiles prior to complete fracture in notched PBS and notched Polydimethylsiloxane (PDMS) elastomer (Lee et al., 2024) specimens. Compared to the trumpet profile for PBS, the elastomer exhibits a single parabola-like fracture profile. The single parabola-like fracture profile for elastomers has been well documented in literature (Qi et al., 2019, Shrivastava et al., 2023). *A fracture model for soft polymers such as the one proposed in this work, in addition to accurately predicting the failure loads, should predict these significantly varying physical phenomena observed in experiments.*

3. Basis for a unique measure of fracture resistance for soft polymers

In permanently crosslinked soft polymers that fracture by crosslink failure, i.e., polymer chain backbone bonds are stronger than crosslinks, it can be assumed that all crosslinks at a material point fail simultaneously (Mao and Anand, 2018a). The weak crosslinks in dynami-

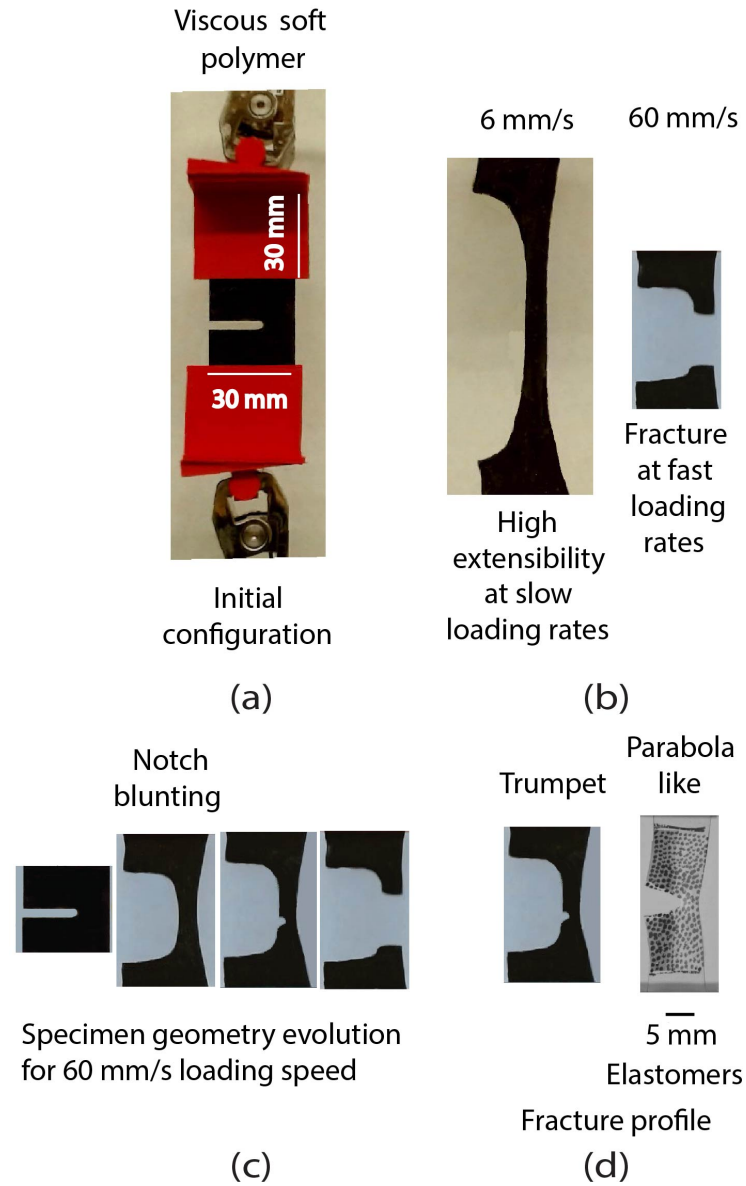


Figure 1: (a) Geometry of a notched PBS specimen and experiment schematic. The thickness of the specimen is 3.2 mm. PBS was colored for visualization. (b) High extensibility of the notched PBS specimen when stretched at a slow loading speed (6 mm/s). Fracture of the specimen at a fast loading speed (60 mm/s). (c) Specimen geometry evolution till complete failure for the 60 mm/s loading speed. Significant notch blunting occurs before notch propagation. (d) Trumpet fracture profile (formation of second local notch ahead of the original blunted notch) in the rapidly stretched notched PBS specimen. A single parabola-like fracture profile experimentally observed in PDMS elastomer (image from J. Lee et al. (2024) (Lee et al., 2024) reproduced with Creative Commons [CC BY-NC-ND 4.0 - <https://creativecommons.org/licenses/by-nc-nd/4.0/>] copyright license).

cally crosslinked soft polymers are constantly breaking and reforming, even in an undeformed state. This dissociation rate is amplified by stretching of the corresponding subchains with respect to the stress-free subchain formation configuration (Song et al., 2021, Venkata et al., 2021). Subchains denote parts of chain molecules between two crosslinks connected to the elastically active network. All subchains in a volume element in a dynamically crosslinked soft polymer can be broken simultaneously only when they are stretched equally to the level corresponding to stretch-induced dissociation. This scenario, however, can occur only at infinitely fast rates, which is not practically feasible. At adequate fast rates, a sufficient number of subchains surviving from close to time $t = 0$ will dissociate from the elastically active network, creating voids. These voids will coalesce and lead to the complete failure of a volume element (Shen et al., 2021). A measure of fracture resistance here can thus be thought of as a critical value of input energy density beyond which network stretching and subsequent damage in the form of stress-accelerated subchain dissociation becomes more dominant than network reconfiguration.

The standard form of referential mechanical power balance for an arbitrary referential volume P (with its surface denoted by ∂P) of a body without the consideration of damage (Gurtin et al., 2010) can be written as

$$\int_{\partial P} t_i^R \dot{\chi}_i da_R + \int_P b_i^R \dot{\chi}_i dv_R = \int_P \left(\frac{1}{2} S_{ij} \dot{C}_{ij} + \frac{1}{2} \rho_R \dot{\chi}_i \dot{\chi}_i \right) dv_R. \quad (3.1)$$

t_i^R , b_i^R are the referential traction and body force vectors respectively. da_R , dv_R are the referential area and volume elements corresponding to ∂P and P , respectively. χ_i is the spatial position of a material point X_i . S_{ij} , $C_{ij} = F_{ki} F_{kj}$ are the second Piola-Kirchoff stress tensor and the right Cauchy-Green deformation tensor, respectively with $F_{ij} = \frac{\partial \chi_i}{\partial X_j}$ being the deformation gradient. Stress work is defined as

$$W(X_i, t) = \int_0^t \frac{1}{2} S_{ij} \dot{C}_{ij} dt, \quad (3.2)$$

quantifies the total energy density per unit referential volume supplied to a material point X_i due to the work done by external macroscopic forces in the scenarios where kinetic energy is negligible. W_{cr} is defined as the value of W , i.e., the total energy per unit referential volume that needs to be supplied for the complete failure of a material point subjected to sufficiently fast loading rates for damage initiation. *Irrespective of the strain rate value under consideration, the same number of bonds have to be broken for the complete failure of a material point.* A common loading mode-based response asymmetry observed in soft polymers is tension-compression asymmetry (Drozdov and deC. Christiansen, 2020, Huang et al., 2016). W_{cr} 's value can then be different in tension and compression for these soft

polymers. However, for a given loading mode, i.e., tension or compression, the hypothesis is that W_{cr} is a unique value with respect to loading rates and specimen geometries. W_{cr} can be evaluated using relatively simple experiments involving homogeneous deformation and without constitutive models. For a uniaxial tensile loading, W_{cr} is equivalent to the standard modulus of toughness, which is defined as the area under engineering stress-strain curve in a uniaxial tensile test till complete specimen failure (Roylance, 2001, Brostow et al., 2015). The unit of W_{cr} is J/m^3 in contrast to J/m^2 for the conventional fracture toughness measures (Yin et al., 2021, Mai and Powell, 1991). The standard energy release rate is the measure of loss of energy per unit area of crack growth (Li et al., 1985, Budiansky and Rice, 1973). It is usually dependent on the constraints created at the crack tip by the amount of material, i.e., specimen dimensions considered (Kang et al., 2005, Zhu and Joyce, 2012). On the contrary, W_{cr} considers the energy density associated with the *complete failure of an arbitrary material point*. Hence, the value of W_{cr} should be independent of specimen dimensions.

We now utilize experimental stress-strain curves for a few soft polymers to demonstrate the negligible dependence of W_{cr} on strain rate. Zhao and co-workers (Zhao et al., 2020b) synthesized a rate-dependent soft polymer with dynamic crosslinks [TFPM-PDMS-25000: 4-[tris(4-formylphenyl)methyl]benzaldehyde (TFPM) used as a tetratopic linker to crosslink PDMS]. The mechanical response of TFPM-PDMS-25000 under uniaxial tensile loading at different stretching speeds was also characterized in the paper. Results are shown in Figure 2(a). We calculated W_{cr} for each loading rate by evaluating the area under the corresponding engineering stress-strain curve. W_{cr} values as a function of strain rate are shown in Figure 2(b). W_{cr} is approximately constant over one decade of strain rate considered. Polyurethane’s (2% w/w of Polyethylene glycol with respect to Palm-based polyol content) rate-dependent mechanical response reported by Somarathna and co-workers Somarathna et al. (2020) is shown in Figure 2(c) with uniaxial tensile engineering stress-strain curves over a range of strain rates. We calculated W_{cr} for each strain rate from the corresponding engineering stress-strain curve. We show that W_{cr} is roughly constant over two decades of strain rate through Figure 2(d). Over this range of strain rate, energy release rate, and crack tip field measures for rate-dependent soft polymers can vary by an order of magnitude or more (Song et al., 2021, Long and Hui, 2016). We also show a negligible variation in W_{cr} value for different loading modes by evaluating W_{cr} from the stress-strain data for Ecoflex elastomer (material has no loading mode-based response asymmetries) reported by Ahmad and co-workers (Ahmad et al., 2019). Results of homogeneous uniaxial tension (UX), pure shear (PS), and equibiaxial tension (EB) tests performed by the authors at a constant engineering strain rate of 0.3 s^{-1} are shown in Figure 2(e). We evaluated W_{cr} for each loading

mode from the corresponding engineering stress-strain curves. W_{cr} is approximately constant for the three loading modes considered: 2 MPa (UX), 1.6 MPa (PS), and 1.7 MPa (EB) as shown in Figure 2(f). These examples further support our hypothesis that within a reasonable approximation, W_{cr} can be used as a scalar measure of fracture resistance of soft polymers.

4. Fracture model

We base our fracture model on the Kroner-Lee (Kröner, 1959, Lee, 1969, Kothari et al., 2019, Niu et al., 2023) multiplicative decomposition of the deformation gradient tensor F_{ij} into elastic and plastic parts F_{ij}^e and F_{ij}^p , respectively and the parallel multi-mechanism generalization of the multiplicative decomposition used in elastic-viscoplastic and viscoelastic constitutive theories for polymers (Boyce et al., 1988, 1989, Vogel et al., 2014, de Rooij and Kuhl, 2016, Bergström and Boyce, 1998, Anand et al., 2009, Ames et al., 2009, Srivastava et al., 2010a,b). An isothermal model is developed for materials that can be idealized as isotropic. For a generalized consideration, M parallel mechanisms of deformation are considered. Damage variables $d^{(q)}(X_i, t) \in [0, 1]$, $q \in [1, M]$ are introduced to model damage and subsequent fracture. We set the general criteria to be $d^{(q)}(X_i, t) = 0$ for undamaged and $d^{(q)}(X_i, t) = 1$ for completely damaged mechanism q at a material point X_i . W_{cr} in a multi-mechanism sense can be interpreted as the value of W when the damage fields for all mechanisms ($d^{(1)}, d^{(2)}, \dots, d^{(M)}$) reach the value of 1 at a material point subjected to loading rates sufficiently fast to cause damage initiation in each mechanism. The method of virtual power is now used to derive the macroscopic and microscopic force balances.

4.1. Method of virtual power for multi-mechanism deformation and damage

The kinematic rate-like descriptors in the framework, while considering M parallel mechanisms of deformation that capture the mechanical response of a material, are taken as

$$\dot{\chi}_i, \dot{F}_{ij}^{e(1)}, \dot{F}_{ij}^{e(2)}, \dots, \dot{F}_{ij}^{e(M)}, \dot{\epsilon}^{p(1)}, \dot{\epsilon}^{p(2)}, \dots, \dot{\epsilon}^{p(M)}, \dot{d}^{(1)}, \dot{d}^{(2)}, \dots, \dot{d}^{(M)}, \frac{\partial \dot{d}^{(1)}}{\partial X_i}, \frac{\partial \dot{d}^{(2)}}{\partial X_i}, \dots, \frac{\partial \dot{d}^{(M)}}{\partial X_i}. \quad (4.1)$$

χ_i is a smooth one-to-one mapping of a material point X_i to its position in the deformed configuration x_i as $x_i = \chi_i(X_1, X_2, X_3, t)$. $F_{ij} = \frac{\partial \chi_i}{\partial X_j}$ is the deformation gradient tensor. $F_{ij}^{e(q)}$ and $F_{ij}^{p(q)}$ are the elastic and plastic parts of F_{ij} in mechanism $q \in [1, M]$ following the multiplicative decomposition $F_{ij} = F_{ik}^{e(q)} F_{kj}^{p(q)}$.

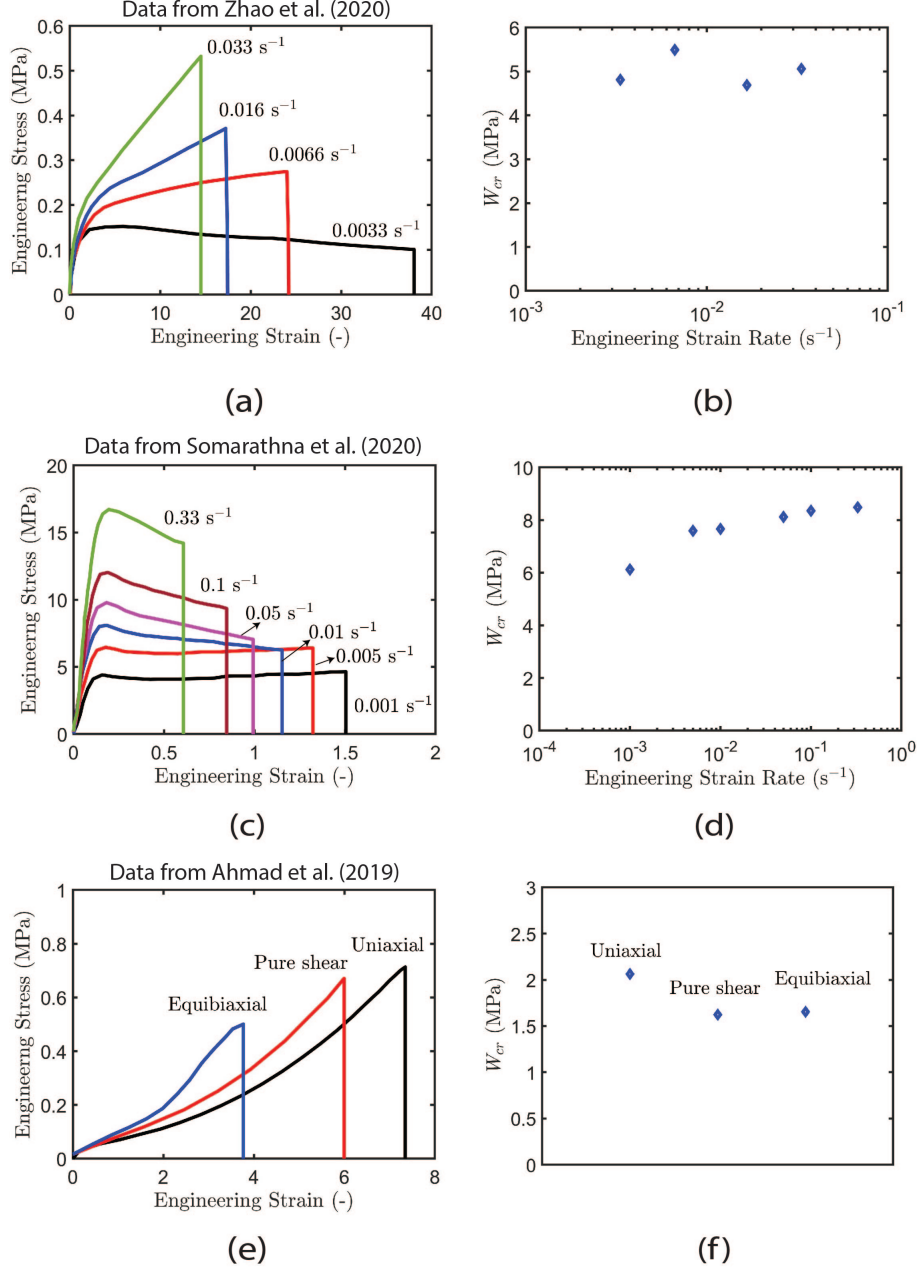


Figure 2: (a) Engineering stress-strain curves at different strain rates for a rate-dependent viscous soft polymer with dynamic crosslinks (TFPM-PDMS-25000) from (Zhao et al., 2020b). (b) W_{cr} evaluated as the area under the stress-strain curve is approximately constant over the decade of strain rate considered. (c), (d) Engineering stress-strain curves for polyurethane from (Somarathna et al., 2020) and roughly constant W_{cr} evaluated over two decades of strain rates, respectively. (e) Uniaxial tension, Pure shear, and Equibiaxial tension engineering stress-strain curves for Ecoflex elastomer at a stretch rate of 0.3 s^{-1} from (Ahmad et al., 2019). (f) Ecoflex's approximately constant W_{cr} evaluated for three different loading modes considered.

$$\begin{aligned}\dot{\epsilon}^{p(q)} &\stackrel{\text{def}}{=} \sqrt{D_{ij}^{p(q)} D_{ij}^{p(q)}}, \quad D_{ij}^{p(q)} = \frac{1}{2} \left(\dot{F}_{ik}^{p(q)} F_{kj}^{p(q)-1} + F_{ki}^{p(q)-1} \dot{F}_{jk}^{p(q)} \right), \\ \epsilon^{p(q)} &\stackrel{\text{def}}{=} \int_0^t \dot{\epsilon}^{p(q)} dt, \quad d^{(q)} \in [0, 1] \quad : q \in [1, M],\end{aligned}\tag{4.2}$$

are a measure of plastic strain rate, plastic stretching tensor corresponding to $F_{ij}^{p(q)}$, a measure of plastic strain, and damage variable respectively for mechanism q . The model is developed for isotropic materials and consequently, the assumption of plastic irrotationality is valid. The definition of velocity gradient L_{ij} ($=\dot{F}_{ik}F_{kj}^{-1}$) and the multiplicative decomposition of F_{ij} result in the following constraints

$$\frac{\partial \dot{\chi}_i}{\partial X_k} F_{kj}^{-1} = \dot{F}_{ik}^{e(q)} F_{kj}^{e(q)-1} + \dot{\epsilon}^{p(q)} F_{ik}^{e(q)} N_{kl}^{p(q)} F_{lj}^{e(q)-1}, \quad N_{ij}^{p(q)} = \frac{D_{ij}^{p(q)}}{\left(\sqrt{D_{kl}^{p(q)} D_{kl}^{p(q)}} \right)} : \forall q \in [1, M],\tag{4.3}$$

where $N_{ij}^{p(q)}$ is the plastic flow direction for mechanism q . Evolution of a reference body B and an arbitrary part of it denoted by P with outward unit normal n_i^R on its boundary ∂P is associated with macroscopic and microscopic force systems. The macroscopic system is defined by (i) traction t_i^R corresponding to n_i^R and generalized body force per unit referential volume b_i^R expending power on $\dot{\chi}_i$. Specifically, $b_i^R = b_i^{0R} - \rho_R \ddot{\chi}_i$, with b_i^{0R} being the conventional body force per unit referential volume, $-\rho_R \ddot{\chi}_i$ representing the inertial body force per unit referential volume, ρ_R denoting the referential mass density and (ii) elastic stress $P_{ij}^{e(q)}$ expending power over the elastic distortion rate $\dot{F}_{ij}^{e(q)}$.

The microscopic system is defined with: (i) scalar microscopic stresses $\pi^{(q)}$ expending power over $\dot{\epsilon}^{p(q)}$, (ii) scalar microscopic stresses $\bar{\omega}^{(q)}$ expending power over $\dot{d}^{(q)}$, (iii) vector microscopic stresses $\xi_i^{(q)}$ expending power over $\frac{\partial \dot{d}^{(q)}}{\partial X_i}$ and (iv) scalar microscopic tractions $\Upsilon^{(q)}(n_i^R)$ expending power over $\dot{d}^{(q)}$ on the part's boundary. For a given P, the power expended on P by the material external to it ($\mathcal{W}_{ext}(P)$) and the power expenditure within P ($\mathcal{W}_{int}(P)$) respectively, can be expressed as

$$\begin{aligned}\mathcal{W}_{ext}(P) &= \int_{\partial P} t_i^R \dot{\chi}_i da_R + \int_P b_i^R \dot{\chi}_i dv_R + \int_{\partial P} \sum_{q=1}^M \left(\Upsilon^{(q)} \dot{d}^{(q)} \right) da_R, \\ \mathcal{W}_{int}(P) &= \int_P \left(\sum_{q=1}^M \left[J^{p(q)} P_{ij}^{e(q)} \dot{F}_{ij}^{e(q)} + J^{p(q)} \pi^{(q)} \dot{\epsilon}^{p(q)} + \bar{\omega}^{(q)} \dot{d}^{(q)} + \xi_i^{(q)} \frac{\partial \dot{d}^{(q)}}{\partial X_i} \right] \right) dv_R.\end{aligned}\tag{4.4}$$

Note that the stress powers $P_{ij}^{e(q)} \dot{F}_{ij}^{e(q)}$, $\pi^{(q)} \dot{\epsilon}^{p(q)}$ in (4.4) are per unit volume ($J^{p(q)}$) of the intermediate space corresponding to $F_{ij}^{p(q)}$. Assuming that the fields $\chi_i, F_{ij}^{e(1)}, F_{ij}^{e(2)}, \dots, F_{ij}^{e(M)}$, $\epsilon^{p(1)}, \epsilon^{p(2)}, \dots, \epsilon^{p(M)}, d^{(1)}, d^{(2)}, \dots, d^{(M)}$ are known at an arbitrarily chosen time instant, the fields $\dot{\chi}_i, \dot{F}_{ij}^{e(1)}, \dot{F}_{ij}^{e(2)}, \dots, \dot{F}_{ij}^{e(M)}, \dot{\epsilon}^{p(1)}, \dot{\epsilon}^{p(2)}, \dots, \dot{\epsilon}^{p(M)}, \dot{d}^{(1)}, \dot{d}^{(2)}, \dots, \dot{d}^{(M)}$ need to be specified independently while satisfying the constraints in (4.3). The generalized virtual velocity can be written as

$$\mathcal{V} = (\tilde{\chi}_i, \tilde{F}_{ij}^{e(1)}, \tilde{F}_{ij}^{e(2)}, \dots, \tilde{F}_{ij}^{e(M)}, \tilde{\epsilon}^{p(1)}, \tilde{\epsilon}^{p(2)}, \dots, \tilde{\epsilon}^{p(M)}, \tilde{d}^{(1)}, \tilde{d}^{(2)}, \dots, \tilde{d}^{(M)}). \quad (4.5)$$

The virtual field \mathcal{V} is rigid if it satisfies

$$(\nabla \tilde{\chi}_i) = \tilde{F}_{ij} = \Omega_{ik} F_{kj}, \quad \tilde{F}_{ij}^{e(q)} = \Omega_{ik} F_{kj}^{e(q)}, \quad \tilde{\epsilon}^{p(q)} = 0, \quad \tilde{d}^{(q)} = 0 : \forall q \in [1, M], \quad (4.6)$$

where Ω_{ij} is a spatially constant skew tensor. Here, $(\tilde{\cdot})$ denotes virtual field quantities. The principle of virtual power requires that

$$\mathcal{W}_{int}(\mathbf{P}, \mathcal{V}) = \mathcal{W}_{ext}(\mathbf{P}, \mathcal{V}) : \forall \mathcal{V} \text{ and } \mathcal{W}_{int}(\mathbf{P}, \mathcal{V}) = 0 : \forall \text{ rigid } \mathcal{V}. \quad (4.7)$$

The total free energy density per unit referential volume ψ_R can be additively decomposed into contributions from each mechanism of deformation and energetic parts accounting for the effects of gradients in the damage fields $\psi^{d(q)}$: $q \in [1, M]$ as

$$\psi_R = \sum_{q=1}^M \left(J^{p(q)} \psi^{(q)} + \psi^{d(q)} \right), \quad T_{ij} = \sum_{q=1}^M T_{ij}^{(q)}, \quad (4.8)$$

where $\psi^{(q)}$ is the contribution from mechanism q per unit volume of the corresponding intermediate space ($J^{p(q)}$). $\psi^{d(q)}$ can be interpreted as defect energy due to local elastic incompatibilities caused by gradients in the damage field variable $d^{(q)}$. This is similar to the interpretation of the free energy contributions due to plastic strain gradients in standard strain-gradient plasticity theories (Lele and Anand, 2009, Reddy, 2011). $T_{ij}, T_{ij}^{(q)}$ are the total Cauchy stress and total Cauchy stress contribution from mechanism q , respectively. The total first Piola-Kirchoff stress P_{ij} , the total second Piola-Kirchoff stress S_{ij} and T_{ij} are related through the following relations

$$P_{ij} = J T_{ik} F_{jk}^{-1} = J \left(\sum_{q=1}^M T_{ik}^{(q)} \right) F_{jk}^{-1} = \sum_{q=1}^M J T_{ik}^{(q)} F_{jk}^{-1} = \sum_{q=1}^M P_{ij}^{(q)}, \quad P_{ij} = F_{ik} S_{kj}, \quad S_{ij} = J F_{ik}^{-1} T_{kl} F_{jl}^{-1}, \quad (4.9)$$

where $P_{ij}^{(q)}$ is the total first Piola-Kirchoff stress contribution from mechanism q .

4.2. Consequences of the method of virtual power: Macroscopic and microscopic stresses for multi-mechanism deformation and damage

The principle of virtual power necessitates that (4.7) is satisfied. To deduce the consequences, any generalized virtual velocity \mathcal{V} consistent with (4.3) can be chosen. Standard procedure and variational arguments to obtain macroscopic and microscopic force balances (Germain, 1973, Gurtin, 1996, 2002, Gurtin et al., 2010, Narayan and Anand, 2019) are followed, and the results are summarized.

4.2.1 Macroscopic stresses

A \mathcal{V} with $\tilde{\epsilon}^{p(q)} \equiv 0$, $\tilde{d}^{(q)} \equiv 0 : \forall q \in [1, M]$ is considered, so that $\frac{\partial \tilde{\chi}_i}{\partial X_j} = \tilde{F}_{ik}^{e(q)} F_{kj}^{p(q)}$. Using (4.9) and standard arguments, (4.7) results in

$$t_i^R = P_{ij} n_j^R, \quad \frac{\partial P_{ij}}{\partial X_j} + b_i^{0R} = \rho_R \ddot{\chi}_i : P_{ij}^{(q)} \stackrel{\text{def}}{=} J^{p(q)} P_{ik}^{e(q)} F_{jk}^{p(q)-1} \forall q \in [1, M]. \quad (4.10)$$

(4.10) represents the standard referential forms of macroscopic traction condition and force balance, respectively. The second requirement of the principle of virtual power as given in (4.7) leads to

$$P_{ik} F_{jk} = F_{ik} P_{jk}, \quad (4.11)$$

which is the standard result obtained from macroscopic moment balance.

4.2.2 Microscopic stresses

(i) Scalar microstresses $\pi^{(q)}$

Next we consider a \mathcal{V} with $\tilde{\chi}_i \equiv 0_i$, $\tilde{d}^{(q)} \equiv 0 : \forall q \in [1, M]$ and arbitrarily chosen $\tilde{\epsilon}^{p(q)} : q \in [1, M]$. Two additional stress measures are defined, (i) Symmetric elastic second Piola-Kirchhoff stress and (ii) Mandel stress, respectively, as

$$S_{ij}^{e(q)} \stackrel{\text{def}}{=} J^{e(q)} F_{ik}^{e(q)-1} T_{kl}^{(q)} F_{jl}^{e(q)-1}, \quad M_{ij}^{e(q)} \stackrel{\text{def}}{=} C_{ik}^{e(q)} S_{kj}^{e(q)} = J^{e(q)} F_{ki}^{e(q)} T_{kl}^{(q)} F_{jl}^{e(q)-1} : \forall q \in [1, M]. \quad (4.12)$$

$C_{ij}^{e(q)} = F_{ki}^{e(q)} F_{kj}^{e(q)}$ is the elastic right Cauchy-Green deformation tensor for mechanism q . The first requirement of the principle of virtual power given in (4.7) results in the microscopic force balance

$$\pi^{(q)} = \left(M_{ij}^{e(q)} + M_{ji}^{e(q)} \right) N_{ij}^{p(q)} \quad \forall q \in [1, M]. \quad (4.13)$$

(ii) Scalar microstresses $\bar{\omega}^{(q)}$ and vector microstresses $\xi_i^{(q)}$

To obtain $\bar{\omega}^{(q)}$ and $\xi_i^{(q)}$, a \mathcal{V} with $\tilde{\epsilon}^{p(q)} \equiv 0 : \forall q \in [1, M]$ and $\tilde{\chi}_i \equiv 0_i$ is considered. Choosing $\tilde{d}^{(q)} : q \in [1, M]$ arbitrarily, (4.7) yields the microscopic traction conditions and force balances respectively as

$$\Upsilon^{(q)} = \xi_i^{(q)} n_i^R, \quad \frac{\partial \xi_i^{(q)}}{\partial X_i} - \bar{\omega}^{(q)} = 0 : \forall q \in [1, M]. \quad (4.14)$$

A set of thermodynamically consistent constitutive equations along with the above macroscopic and microscopic force balances give the complete set of governing mechanical equations for the model. The internal power expenditure in (4.4) can now be rewritten using (4.12) as

$$\mathcal{W}_{int}(P) = \int_P \left(\sum_{q=1}^M \left[\frac{1}{2} J^{p(q)} S_{ij}^{e(q)} \dot{C}_{ij}^{e(q)} + J^{p(q)} \pi^{(q)} \dot{\epsilon}^{p(q)} + \bar{\omega}^{(q)} \dot{d}^{(q)} + \xi_i^{(q)} \frac{\partial \dot{d}^{(q)}}{\partial X_i} \right] \right) dv_R. \quad (4.15)$$

4.3. Free energy imbalance

Under isothermal conditions, the local form of free energy imbalance can be finally expressed as

$$\dot{\psi}_R - \sum_{q=1}^M \left(\frac{1}{2} J^{p(q)} S_{ij}^{e(q)} \dot{C}_{ij}^{e(q)} + J^{p(q)} \pi^{(q)} \dot{\epsilon}^{p(q)} + \bar{\omega}^{(q)} \dot{d}^{(q)} + \xi_i^{(q)} \frac{\partial \dot{d}^{(q)}}{\partial X_i} \right) \leq 0. \quad (4.16)$$

We note here that all the terms involved in (4.16) are frame invariant.

4.4. Constitutive equations for deformation and damage

Using (4.8), the free energy imbalance in (4.16) can be written as

$$\begin{aligned} & \sum_{q=1}^M \left(J^{p(q)} \left(\frac{\partial \hat{\psi}^{(q)}(\Lambda^{(q)})}{\partial C_{ij}^{e(q)}} - \frac{1}{2} S_{ij}^{e(q)} \right) \dot{C}_{ij}^{e(q)} - J^{p(q)} \left(\pi^{(q)} - \frac{\partial \hat{\psi}^{(q)}(\Lambda^{(q)})}{\partial \epsilon^{p(q)}} \right) \dot{\epsilon}^{p(q)} - \left(\bar{\omega}^{(q)} - \frac{\partial \tilde{\psi}_R(\Lambda)}{\partial d^{(q)}} \right) \dot{d}^{(q)} \right. \\ & \left. - \left(\xi_i^{(q)} - \frac{\partial \tilde{\psi}_R(\Lambda)}{\partial d^{(q)}} \right) \frac{\partial \dot{d}^{(q)}}{\partial X_i} \right) \leq 0. \end{aligned} \quad (4.17)$$

where

$$\Lambda^{(q)} = \left(C_{ij}^{e(q)}, \epsilon^{p(q)}, d^{(q)}, \frac{\partial d^{(q)}}{\partial X_i} \right) \quad q \in [1, M], \quad \Lambda = (\Lambda^{(1)}, \Lambda^{(2)}, \dots, \Lambda^{(M)}), \quad (4.18)$$

are generalized lists of variables. $\psi^{d^{(q)}}$ is taken to be dependent on $d^{(q)}, \frac{\partial d^{(q)}}{\partial X_i}$. The following state relations are assumed

$$S_{ij}^{e(q)} = 2 \frac{\partial \hat{\psi}^{(q)}(\Lambda^{(q)})}{\partial C_{ij}^{e(i)}}, \quad \xi_i^{(q)} = \frac{\partial \tilde{\psi}_R(\Lambda)}{\partial \left(\frac{\partial \dot{d}^{(q)}}{\partial X_i} \right)}, \quad \pi_{en}^{(q)} = \frac{\partial \hat{\psi}^{(q)}(\Lambda^{(q)})}{\partial \epsilon^{p(q)}}, \quad \bar{\omega}_{en}^{(q)} = \frac{\partial \tilde{\psi}_R(\Lambda)}{\partial d^{(q)}} : \forall q \in [1, M], \quad (4.19)$$

with $\pi^{(q)} = \pi_{en}^{(q)} + \pi_{dis}^{(q)}$, $\bar{\omega}^{(q)} = \bar{\omega}_{en}^{(q)} + \bar{\omega}_{dis}^{(q)}$. The subscripts *en* and *dis* denote energetic and dissipative parts, respectively. To satisfy the dissipation inequality in (4.17), it is assumed that

$$\pi_{dis}^{(q)} \epsilon^{p(q)} \geq 0, \quad \bar{\omega}_{dis}^{(q)} \dot{d}^{(q)} \geq 0 \quad \forall q \in [1, M]. \quad (4.20)$$

4.5. Free energy specialization for PBS

The total referential free energy density ψ_R in (4.8) is taken to be in the following specific form for PBS

$$\psi_R = g(d) \psi_o^+ + \psi_o^- + \underbrace{\psi_* l^2 \left(\frac{\partial^2 d}{\partial X_i \partial X_i} \right)^2}_{\psi^d}, \quad \psi_o = \sum_{q=1}^{M=2} \psi_o^{(q)}, \quad (4.21)$$

where $\psi_* > 0$ is a coefficient with units of energy per unit volume, and $l > 0$ is a length scale parameter that controls the spread of the diffused damage zone. The same damage field variable is used for all mechanisms in PBS to reflect the experimentally observed single load drop corresponding to fracture in Figure 4(b) for the notched tension test. In the case of multiple load drops observation (King, 2022, Imaoka et al., 2023), different damage variables corresponding to different underlying mechanisms of deformation need to be used. Some works on fracture modeling of composites have incorporated multiple damage variables to account for matrix and filler damage separately (Zhang et al., 2022, Jihai Yuan and Chen, 2022, Li et al., 2024).

ψ_o is the total undamaged elastic free energy which is the additive decomposition of contributions $(\psi_o^{(q)})^2$ from the two ($M = 2$) main mechanisms of deformation in PBS over the loading timescales considered in this work. ψ_o^- is the part of ψ_o which is dilatational and compressive. $\psi_o^+ = \psi_o - \psi_o^-$ is the damage driving part of ψ_o . This split accounts for damage growth being driven only by distortional and tensile dilatational deformation (Amor et al., 2009, Hesammokri et al., 2023). The two mechanisms of deformation are: (a) **Intermolecular Resistance (A)**: Elastic and dissipative resistance due to intermolecular

²Any suitable free energy density function of choice can be used here for a specific soft polymer under consideration.

interactions between neighboring molecules. (b) **Network Resistance (B)**: stretching of constituent subchains within Boron(B):Oxygen(O) coordinate-bond dynamic crosslinks (Konale et al., 2023).

Specifically, ψ_o is taken as

$$\begin{aligned} \psi_o &= \underbrace{\psi_o^{(A)}}_{\text{Intermolecular resistance}} + \underbrace{\psi_o^{(B)}}_{\text{Network resistance}}, \\ &= \underbrace{G \left(E_{ij}^{e(A)'} E_{ij}^{e(A)'} \right) + \frac{1}{2} K \left(E_{kk}^{e(A)} \right)^2}_{\psi_o^{(A)}} \\ &\quad + \underbrace{\mu \bar{\lambda}_L^2 \left(e^{-k_{ns}t} \zeta(t/0) + \int_0^t \frac{n_{ns}}{n_s} k_s e^{-k_{ns}(t-t')} \zeta(t/t') dt' \right)}_{\psi_o^{(B)}}, \end{aligned} \quad (4.22)$$

with $\zeta(t/t') = \left[\left(\frac{\bar{\lambda}(t/t')}{\bar{\lambda}_L} \right) \beta(t/t') + \ln \left(\frac{\beta(t/t')}{\sinh \beta(t/t')} \right) \right]$.³ Plastic incompressibility is assumed for mechanism A. The referential number density of chain segments currently in their subchain state (S) and that of chain segments that can be in the subchain state, but are not currently (NS) are denoted by n_s and n_{ns} , respectively. The underlying dynamic, reversible reactions can be represented as



where k_s and k_{ns} are the forward and backward reaction rate parameters, respectively. Setting $G = k_{ns} = k_s = 0$ in (4.22) results in $\psi_o = \mu \bar{\lambda}_L^2 \zeta(t/0)$, which is the eight-chain free energy density function (Arruda and Boyce, 1993) used for elastomers. The effect of k_{ns} 's value on the mechanical response can be understood easily by setting $G = 0$ in (4.22) to get $\psi_o = \psi_o^{(B)}$.⁵ Kinematic quantities with notation (t/t') use the relative deformation gradient: $F_{ij}(t/t') = F_{ik}(t) F_{kj}^{-1}(t')$, a temporal decomposition of F_{ij} , which maps the

³ $\bar{\lambda}_L$ is the network locking stretch parameter accounting for finite chain extensibility. The effective total distortional stretch $\bar{\lambda}$ is defined as $\bar{\lambda} \stackrel{\text{def}}{=} \sqrt{\frac{C_{kk}^*}{3}}$ with C_{ij}^* being the distortional part of C_{ij} . $\beta = \mathcal{L}^{-1} \left(\frac{\bar{\lambda}}{\bar{\lambda}_L} \right)$ and $\mathcal{L}(\cdot) = \coth(\cdot) - \frac{1}{(\cdot)}$ denotes the Langevin function. $G > 0$, $K > 0$ are the shear and bulk moduli respectively. $E_{ij}^{e(A)'} = \ln U_{ij}^{e(A)}$ is an elastic logarithmic strain measure, where $U_{ij}^{e(A)}$ is the right elastic stretch tensor following the polar decomposition of $F_{ij}^{e(A)}$. A_{ij}' denotes the deviatoric part of a tensor A_{ij} .

⁴ $\mu = n_s k_B \theta$ denotes the ground state shear modulus with k_B , θ denoting the Boltzmann constant and temperature respectively.

⁵The proposed constitutive model can be used as a general model for a broad class of soft polymers with response varying from elastic to significantly viscous. At any given time instant, smaller values of k_{ns}

deformed configuration at t' to the deformed configuration at t as the input. This accounts for subchains formed at t' ($0 < t' < t$) and surviving till the current time t being stretched with respect to their stress-free, relaxed configurations corresponding to t' . We note that $\psi_o^{(B)}$ is purely deviatoric, while $\psi_o^{(A)}$ has a deviatoric part i.e. $G \left(E_{ij}^{e(A)'} E_{ij}^{e(A)'} \right)$ and a dilatational part i.e. $\frac{1}{2}K \left(E_{kk}^{e(A)} \right)^2$. If $E_{kk}^{e(A)} > 0$, i.e., tensile dilatation, $\psi_o^+ = \psi_o$ ($\psi_o^{(A)+} = \psi_o^{(A)}$) and $\psi_o^- = \psi_o^{(A)-} = 0$. On the other hand, if $E_{kk}^{e(A)} < 0$, i.e., compressive dilatation, $\psi_o^+ = \left[\psi_o^{(A)+} = G \left(E_{ij}^{e(A)'} E_{ij}^{e(A)'} \right) \right] + \psi_o^{(B)}$ and $\psi_o^- = \psi_o^{(A)-} = \frac{1}{2}K \left(E_{kk}^{e(A)} \right)^2$.

The monotonically decreasing function $g(d)$, which degrades the energy storage with damage growth at a material point, is taken as (Miehe et al., 2010a, Mao et al., 2017, Anand et al., 2019, Konica and Sain, 2021, Narayan and Anand, 2021)

$$g(d) = (1 - d)^2. \quad (4.24)$$

The total Cauchy stress is given as

$$\begin{aligned} T_{ij} &= g(d) \left[\underbrace{T_{ij}^{(A)o+} + T_{ij}^{(B)o}}_{T_{ij}^{o+}} \right] + \underbrace{T_{ij}^{(A)o-}}_{T_{ij}^{o-}}, \\ \text{if } E_{mm}^{e(A)} < 0 : T_{ij}^{(A)o+} &= J^{-1} R_{ik}^{e(A)} \left(2G E_{kl}^{e(A)'} \right) R_{jl}^{e(A)}, \\ T_{ij}^{(A)o-} &= J^{-1} R_{ik}^{e(A)} \left(K E_{mm}^{e(A)} \delta_{kl} \right) R_{jl}^{e(A)}, \\ \text{else : } T_{ij}^{(A)o+} &= J^{-1} R_{ik}^{e(A)} \left(2G E_{kl}^{e(A)'} + K E_{mm}^{e(A)} \delta_{kl} \right) R_{jl}^{e(A)}, \\ T_{ij}^{(A)o-} &= 0, \\ T_{ij}^{(B)o} &= e^{-k_{ns}t} \mu \Gamma_{ij}(t/0) + \int_0^t \frac{n_{ns}}{n_s} k_s e^{-k_{ns}(t-t')} \mu \Gamma_{ij}(t/t') dt'. \end{aligned} \quad (4.25)$$

$T_{ij}^o = T_{ij}^{o+} + T_{ij}^{o-}$ is the undamaged total Cauchy stress. T_{ij}^{o+} , T_{ij}^{o-} are the undamaged total Cauchy stress contributions corresponding to ψ_o^+ , ψ_o^- respectively. $T_{ij}^{(A)o} = T_{ij}^{(A)o+} + T_{ij}^{(A)o-}$ and $T_{ij}^{(B)o}$ are the undamaged total Cauchy stress contributions from mechanisms A ($\psi_o^{(A)} = \psi_o^{(A)+} + \psi_o^{(A)-}$) and B ($\psi_o^{(B)}$) respectively (Konale et al., 2023). $\Gamma_{ij}(t/t') = J^{-1}(t/t') \frac{\bar{\lambda}_L}{\bar{\lambda}(t/t')} \mathcal{L}^{-1} \left[\frac{\bar{\lambda}(t/t')}{\bar{\lambda}_L} \right] B_{ij}^{*'}(t/t')$ ⁶. *This constitutive model can be applied to a variety*

will result in ψ_o tending to the eight-chain form $\mu \bar{\lambda}_L^2 \zeta(t/0)$, i.e., elastomer-like behavior with insignificant network reconfiguration. On the other hand, higher values of k_{ns} will lead to the departure of ψ_o from the elastic behavior to significantly viscous behavior with appreciable network reconfiguration.

⁶ $B_{ij} = F_{ik} F_{jk}$ is the total left Cauchy-Green deformation tensor.

of polymers ranging from elastomers to highly viscous soft polymers by suitably adjusting the model parameters, especially the crosslink macroscopic relaxation and formation timescales..

4.6. Viscous flow rule for Mechanism A

Assuming plastic irrotationality, plastic incompressibility, and codirectionality of plastic flow, the plastic stretching tensor $D_{ij}^{p(A)}$ can be expressed as

$$D_{ij}^{p(A)} = \nu^{p(A)} \left(\frac{M_{ij}^{e(A)'}}{2\bar{\tau}^{(A)}} \right), \quad \nu^{p(A)} \stackrel{\text{def}}{=} \sqrt{2} \sqrt{D_{ij}^{p(A)} D_{ij}^{p(A)}}, \quad \bar{\tau}^{(A)} \stackrel{\text{def}}{=} \frac{1}{\sqrt{2}} \sqrt{M_{ij}^{e(A)'}} M_{ij}^{e(A)'}, \quad (4.26)$$

where $\nu^{p(A)}$, $\bar{\tau}^{(A)}$ are the equivalent plastic shear strain rate and the equivalent shear stress, respectively. With $\gamma^{p(A)} \stackrel{\text{def}}{=} \int_0^t \nu^{p(A)} dt$ being an equivalent plastic shear strain rate, we have $\nu^{p(A)} = \sqrt{2} \dot{\epsilon}^{p(A)}$, $\gamma^{p(A)} = \sqrt{2} \epsilon^{p(A)}$. Instead of $\dot{\epsilon}^{p(A)}$, we use $\nu^{p(A)}$ as the rate-like kinematic descriptor. The expression for $\pi^{(A)}$ in (4.13) will have to be divided by $\sqrt{2}$ to account for the change of $\dot{\epsilon}^{p(A)}$ to $\nu^{p(A)}$ as the kinematic descriptor. Using (4.13) and (4.26), we have $\bar{\tau}^{(A)} = \pi^{(A)} = \pi_{dis}^{(A)} + \pi_{en}^{(A)}$. Further, following the specific form for $\psi^{(A)} = g(d)\psi_o^{(A)+} + \psi_o^{(A)-}$ chosen in the main text of the paper and (4.19), $\pi_{en}^{(A)}$ is equal to zero, i.e., $\bar{\tau}^{(A)} = \pi_{dis}^{(A)}$. The microstress $\pi_{dis}^{(A)}$ is assumed to obey the constitutive relation

$$\pi_{dis}^{(A)} = g(d) \mathcal{S}(C_{ij}^{e(A)}, \nu^{p(A)}) \quad \text{when } \nu^{p(A)} > 0. \quad (4.27)$$

In order to satisfy the dissipation inequality in (4.20), we require $\mathcal{S}(C_{ij}^{e(A)}, \nu^{p(A)})$ to be non-negative.

Further, it is assumed that \mathcal{S} depends on $C_{ij}^{e(A)}$ only through $\hat{p}^{(A)} = -K E_{kk}^{e(A)}$
 $= -K \left(\frac{1}{2} \text{trace}(\ln C_{ij}^{e(A)}) \right)$. Also, $\hat{p}^{(A)} = \frac{\bar{p}^{(A)}}{g(d)}$ with $\bar{p}^{(A)} \stackrel{\text{def}}{=} -\frac{1}{3} M_{kk}^{e(A)}$. $\mathcal{S}(C_{ij}^{e(A)}, \nu^{p(A)})$ is chosen to follow a specific form as

$$\mathcal{S}(C_{ij}^{e(A)}, \nu^{p(A)}) = \alpha_p \hat{p}^{(A)} + \mathbb{S} \sinh^{-1} \left[\left(\frac{\nu^{p(A)}}{\nu_0} \right)^m \right], \quad (4.28)$$

where $\alpha_p \geq 0$ is a pressure sensitivity parameter. The last term in (4.28) represents a rate-dependent resistance to plastic flow. \mathbb{S} is an internal variable that models the dissipative friction-like resistance due to the sliding chains. $\nu_0 > 0$ is a reference strain rate and $m \in (0, 1]$ is a strain rate sensitivity parameter. The evolution equation for \mathbb{S} is taken as $\dot{\mathbb{S}} = h(\bar{\lambda} - 1) \nu$ with initial value $\mathbb{S}(X_i, 0) = \mathbb{S}_0 > 0$. h is a stress-dimensional material parameter and $\nu \stackrel{\text{def}}{=} \sqrt{2} \sqrt{D_{ij}^i D_{ij}^i}$ is the total equivalent shear strain rate. The strength relation in (4.27) can now be concisely expressed as

$$\nu^{p(A)} = \begin{cases} 0 & \text{if } \bar{\tau}_e^{(A)} \leq 0, \\ \nu_0 \left[\sinh \left(\frac{\bar{\tau}_e^{(A)}}{g(d)\mathcal{S}} \right) \right]^{1/m} & \text{if } \bar{\tau}_e^{(A)} > 0, \end{cases} \quad (4.29)$$

where $\bar{\tau}_e^{(A)} \stackrel{\text{def}}{=} \bar{\tau}^{(A)} - \alpha_p \bar{p}^{(A)}$ denotes a net equivalent shear stress for plastic flow.

4.7. Evolution equation for damage variable d

The microstructural changes leading to damage in soft polymers like PBS that exhibit dynamic crosslinking are thought to be reversible, i.e., failure of weak dynamic, reversible crosslinks (Song et al., 2021, Shen et al., 2021, Shen and Vernerey, 2020). However, *short timescales for complete damage growth* with respect to the dynamic crosslink macroscopic formation timescale (τ_f) would suggest that damage, if initiated, will grow monotonically. Specimen geometry and experiment schematic for a notched tension test performed at 60 mm/s loading speed are shown in Figure 4(b). The sharp load drop corresponding to fracture in Figure 4(b) for the notched PBS specimen (τ_f is in the order of seconds for PBS (Konale et al., 2023)) highlights the rapid damage growth in PBS. Therefore, we adhere to the modeling approach used for irreversible damage growth (Narayan and Anand, 2019, Konica and Sain, 2021).

Following Narayan and Anand (Narayan and Anand, 2019), the scalar microstress $\bar{\omega}_{dis}$ is expressed as

$$\bar{\omega}_{dis} = \alpha + \zeta \dot{d} : \alpha = 2(1-d)\psi_{cr}^+ + 2\psi_* d > 0 \text{ with } \psi_{cr}^+ > 0, \psi_* > 0. \quad (4.30)$$

where ψ^* , ψ_{cr}^+ are coefficients with units of energy per unit volume, and $\zeta > 0$ is a constant kinetic modulus so that the dissipation inequality is satisfied when $\dot{d} > 0$. The timescale for damage growth is determined by ζ with decreasing values of ζ leading towards rate-independent damage evolution. $\psi_{cr}^+ + \psi_*$ represents a part of the energy dissipated per unit volume as d grows from 0 to 1. The microforce balance in (4.14) along with (4.19) and (4.30) gives the evolution equation for d as

$$\zeta \dot{d} = 2(1-d)\mathcal{H} - 2\psi_* \left(d - l^2 \frac{\partial^2 d}{\partial X_i \partial X_i} \right) : \mathcal{H}(t) \stackrel{\text{def}}{=} \max_{s \in [0, t]} [\langle \psi_o^+(s) - \psi_{cr}^+ \rangle]. \quad (4.31)$$

$\dot{d} \geq 0$ and $d \in [0, 1]$ are ensured by using a monotonically increasing history function \mathcal{H} (Miehe et al., 2010a, Talamini et al., 2018, Narayan and Anand, 2019). The damage initiates only when the damage driving ψ_o^+ reaches the critical value ψ_{cr}^+ . A robust damage initiation

criterion can be imposed by further requiring $\psi_o^{(B)} = \psi_{cr}^{(B)}$ and can be achieved ⁷ using a modified Macauley bracket as

$$\langle x \rangle = \begin{cases} 0 & \text{if } x < 0, \\ x & \text{if } x \geq 0 \text{ and } \psi_o^{(B)} \geq \psi_{cr}^{(B)}. \end{cases} \quad (4.32)$$

In this paper, we have focused on fracture under an overall tensile loading. For soft polymers with tension-compression response asymmetry, different values for the parameter set $\{\psi_{cr}^+, \psi_*, l, \zeta\}$ can be used under compressive loading. This change of parameter values can be triggered using the field variable, which governs the tension-compression response asymmetry in the constitutive model.

5. Parameters in the fracture model

The set of model parameters to be calibrated are

$$\underbrace{\{k_s, k_{ns}, n_s, G, K, \nu_0, m, \alpha_p, S_0, h, \bar{\lambda}_L\}}_{\text{deformation}}, \underbrace{\{\psi_{cr}^+, \psi_{cr}^{(B)}, W_{cr}, \psi_*, l, \zeta\}}_{\text{damage}}. \quad (5.1)$$

Values for all the deformation-associated parameters are taken from Konale and co-workers (Konale et al., 2023).

Uniaxial homogeneous tension tests can be used for evaluation of W_{cr} , ψ_{cr}^+ and $\psi_{cr}^{(B)}$ ⁸. Dogbone tensile PBS specimens of ASTM D638 Type V standard [gauge dimensions: 9.53 ± 1 mm x 3.2 ± 1 mm x 3.2 ± 1 mm] (International, 2015) were subjected to a stretching speed of 60 mm/s. Displacement was monitored through markers at the two extremes of the gauge length and standard image processing. (3.2) for this loading can be written as

$$W(X_i, t) = \int_0^t s \dot{\lambda} dt \quad (5.2)$$

⁷A macroscopic stretch measure, e.g., $\bar{\lambda}(t/0)$ by itself cannot be used as a criterion for damage initiation. This can be understood by considering a loading rate much slower than the dynamic crosslink macroscopic relaxation timescale (τ_r). In this case, the polymer network can easily reconfigure. Even when a specimen is subjected to large global deformation, the subchains, due to continuous network reconfigurations, will be stretched by an insignificant amount. For loading rates much faster than τ_r , the polymer network will not have sufficient time to reconfigure, and the subchains will undergo a significant amount of stretching upon large specimen deformation. Hence, to capture the extent of subchain stretching, $\bar{\lambda}(t/0)$ will have to be further supplemented with a measure of loading rate, e.g., $\dot{\bar{\lambda}}(t/0)$. $\bar{\lambda}(t/0)_{cr}$ will then not be a unique value but dependent on $\dot{\bar{\lambda}}(t/0)$. In contrast, ψ_{cr}^+ and $\psi_{cr}^{(B)}$ are unique values.

⁸Soft polymers exhibit fast damage evolution through sharp load drops corresponding to fracture (Liu et al., 2019b, Zhao et al., 2020b). Hence, W_{cr} for soft polymers will be approximately equal to the value of W at damage initiation ($\psi_o^+ = \psi_{cr}^+$). For hyperelastic materials, $W_{cr} = \psi_{cr}^+$, i.e., there are no viscous contributions to W . $W_{cr} > \psi_{cr}^+$ for materials with viscous effects.

where s , λ are the engineering stress and gauge section stretch in the direction of loading respectively⁹. $\dot{\lambda}$ was evaluated to be 4 s^{-1} and the corresponding σ vs t curve is shown in Figure 4(a). $W_{cr} = 0.6 \text{ MPa}$ was calculated using (5.2) with the integration carried till the time instant of complete failure. A one-dimensional version of the model without considering damage was implemented in MATLAB to simulate this experiment and calculate ψ_o^+ and $\psi_o^{(B)}$. $\psi_{cr}^+ = 0.27 \text{ MPa}$, $\psi_{cr}^{(B)} = 0.12 \text{ MPa}$ were obtained as the values of ψ_o^+ , $\psi_o^{(B)}$ at complete failure.

Although the parameters ψ_* , l , ζ can be fit to the uniaxial tensile test, sensitivity to damage gradients can only be obtained with inhomogeneous deformations, e.g., the notched tension test in Figure 4(b). The model was implemented in the finite element software ABAQUS which has been acceptably used for engineering simulations involving complex loadings, inhomogeneous deformations, and nonlinear material responses (Konica et al., 2024, Niu and Srivastava, 2022a, Vaishakh et al., 2024, Niu and Srivastava, 2022b, Bai et al., 2021, Zhong and Srivastava, 2021, Srivastava et al., 2011). The finite element mesh with a total of 32,468 C3D8R (three-dimensional, reduced integration) used for simulating the notched tension experiment is shown in Figure 4(b). In all the simulations in this work, finer mesh was applied in the regions surrounding the notch to capture the stress and strain gradients. The actual value of the length scale associated with the damage process zone in PBS hasn't been experimentally measured so far. Hence, the length scale parameter l controlling the spread of the diffuse damage zone is considered to be an adjustable regularization parameter. $l = 2.5 \text{ mm}$ was chosen to result in a computationally tractable mesh given the specimen dimensions while following the restriction of $l \gtrsim 5h_e$ (Narayan and Anand, 2021) and being in the range of damage process zone length scales reported for soft polymers (Matsuda et al., 2020, Long et al., 2021, Slotman et al., 2022). ψ_* and ζ were calibrated to fit the load-displacement curve after the load maximum in the notched tension calibration experiment. Model fit to the experimental extension force-displacement curve corresponding to the notched tension test is shown in Figure 4(b). Values of the model parameters are listed in Table 1.

5.1. Finite element implementation of the damage model

The damage variable d is an additional degree of freedom at each node along with displacement. Therefore, implementation in the finite element software ABAQUS requires the development of user-defined elements. Since the timescales involved are short, explicit for-

⁹Analytical expressions for W_{cr} in the case of uniaxial tension can be obtained for hyperelastic materials using (5.2). E.g., if neo-Hookean model is used: $W_{cr} = \mu(\frac{\lambda_{cr}^2}{2} + \frac{1}{\lambda_{cr}} - \frac{3}{2})$, if Mooney-Rivlin model is used: $W_{cr} = 2C_1(\frac{\lambda_{cr}^2}{2} + \frac{1}{\lambda_{cr}} - \frac{3}{2}) + 2C_2(\lambda_{cr} + \frac{1}{2\lambda_{cr}^2} - \frac{3}{2})$ where C_1 , C_2 are material constants and the ground state shear modulus $\mu = 2(C_1 + C_2)$.

Deformation	
Parameter	PBS
k_s (s ⁻¹)	0.35
k_{ns} (s ⁻¹)	0.35
n_s (m ⁻³)	6.4 x 10 ²⁴
G (MPa)	0.4
K (MPa)	20
ν_0 (s ⁻¹)	2 x 10 ⁻³
m (-)	0.95
α_p (-)	0.11
S_0 (kPa)	0.6
h (kPa)	37.7
$\bar{\lambda}_L$ (-)	37.4
ρ_R (kg m ⁻³)	1100
Damage	
ψ_{cr}^+ (MPa)	0.27
$\psi_{cr}^{(B)}$ (MPa)	0.12
W_{cr} (MPa)	0.6
ψ_* (kPa)	4
l (mm)	2.5
ζ (kPa.s)	1.1

Table 1: Model parameters for PBS.

mulation was used, and correspondingly, a VUEL (user-defined element with explicit formulation) was developed. Following the recent works outlining the numerical implementation of phase fields models using VUEL (Wang et al., 2020, Yuan et al., 2022, Hai et al., 2024), we split the problem computationally into (i) a mechanical problem (VUMAT, user-defined mechanical material behavior with inbuilt elements) and (ii) a problem corresponding to the additional degree of freedom d (VUEL). The evolution of d at a node is dependent upon quantities evaluated in the mechanical problem (VUMAT), specifically the damage driving history function \mathcal{H} at the corresponding material (integration) points. Further, to update the total Cauchy stress T_{ij} at a material point, d evaluated from the damage problem (VUEL) at the corresponding nodes is required. This information is passed between VUMAT and VUEL using global variables and the VUSDFLD subroutine. The finite element implementation workflow is summarized in Figure 3.

5.2. Numerical update procedure for $T_{ij}^{(B)o}$ and $\psi_o^{(B)}$

The finite element program ABAQUS returns only the deformation gradients from the previous and current time steps at each material point. Direct numerical implementation

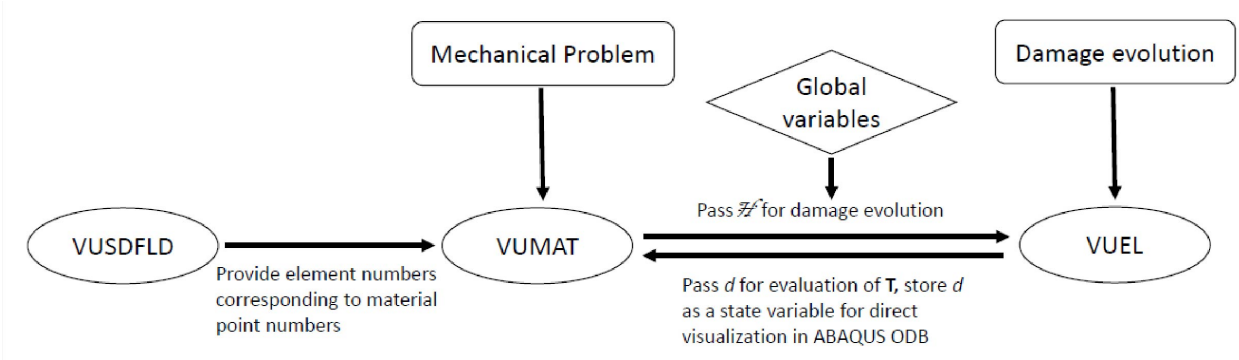


Figure 3: Summary of the finite element implementation workflow. \mathbf{T} denotes the total Cauchy stress tensor T_{ij} .

of the analytical expressions for $T_{ij}^{(B)o}$ and $\psi_o^{(B)}$ in ABAQUS will require the storage of the entire deformation gradient history along with many state-dependent variables at each material point. The resulting storage requirement will be huge, making it challenging. A numerical update procedure for $T_{ij}^{(B)o}$ developed by Konale and co-workers (Konale et al., 2023) is applied, which requires deformation gradients only from the previous and current time steps at each material point. It is summarized as

$$\begin{aligned}
T_{ij}^{(B)o}(t + \Delta t) &\rightarrow e^{-k_{ns}(t+\Delta t)} \mu \Gamma_{ij}(t + \Delta t/0) + T_{ij}^{(B)o2}(t + \Delta t), \\
T_{ij}^{(B)o2}(t + \Delta t) &\rightarrow e^{-k_{ns}\Delta t} J^{-5/3}(t + \Delta t/t) F_{ik}(t + \Delta t/t) T_{kl}^{(B)o2}(t) F_{jl}(t + \Delta t/t) \\
&+ \frac{1}{2} \frac{n_{ns}}{n_s} k_s e^{-k_{ns}\Delta t} \mu \Gamma_{ij}(t + \Delta t/t) \Delta t.
\end{aligned} \tag{5.3}$$

We apply the procedure to $\psi_o^{(B)}$ which can be summarized as

$$\begin{aligned}
\psi_o^{(B)}(t + \Delta t) &\rightarrow e^{-k_{ns}(t+\Delta t)} \mu [\bar{\lambda}_L]^2 \zeta(t + \Delta t/0) + \psi_{o2}^{(B)}(t + \Delta t) - \mu [\bar{\lambda}_L]^2 \zeta(0), \\
\psi_{o2}^{(B)}(t + \Delta t) &\rightarrow e^{-k_{ns}\Delta t} \psi_{o2}^{(B)}(t) + \frac{1}{2} \left[\left(\frac{n_{ns}}{n_s} k_s e^{-k_{ns}\Delta t} \mu [\bar{\lambda}_L]^2 \zeta(t + \Delta t/t) \right) \right. \\
&\left. + \left(\frac{n_{ns}}{n_s} k_s \mu [\bar{\lambda}_L]^2 \zeta(t + \Delta t/t + \Delta t) \right) \right] \Delta t.
\end{aligned} \tag{5.4}$$

5.3. Finite element model reduction using symmetries

For all simulations in this paper, the bottom surface of the specimen is completely fixed, i.e., $u_X = u_Y = u_Z = u_X^R = u_Y^R = u_Z^R = 0$. u , u_R denote the translational and rotational

degrees of freedom of a material point about the axis indicated in the subscript. Z and Y axes are parallel to the thickness and height of the specimen, respectively. For quarter block simulations, $u_X = u_Y^R = u_Z^R = 0$ is prescribed on the symmetry surface with normal along X axis. For both quarter and half block simulations, $u_Z = u_X^R = u_Y^R = 0$ is prescribed on the symmetry surface with normal along the Z axis. Finally, for all simulations, u_Y corresponding to the loading profile is prescribed along with $u_X = u_Z = u_X^R = u_Y^R = u_Z^R = 0$ on the specimen's top surface.

5.4. Estimate of subchain dissociation energy using ψ_{cr}^+

The referential number density of subchains in PBS surviving from $t=0$ till any time instant t ($n_s(t/0)$) can be obtained using the first order kinetics of underlying dynamic reactions (Konale et al., 2023) as equal to $n_s e^{-k_{ns}t}$. At the time instant corresponding to the load drop in Figure 4(a) for the uniaxial tension test, with $k_{ns} = 0.35 \text{ s}^{-1}$ and $n_s = 6.4 \times 10^{24} \text{ m}^{-3}$, $n_s(t/0)$ is equal to $4.7 \times 10^{24} \text{ m}^{-3}$. These subchains experience the highest level of stretch and, hence, will be most likely to undergo stretch-induced dissociation. Hence, it can be assumed that the energy associated with dissociation of $4.7 \times 10^{24} \text{ m}^{-3}$ subchains at a material point is $\psi_{cr}^{(B)}$. The subchain dissociation energy can then be estimated as 15 kJ/mol. We independently conducted oscillatory rheology experiments on PBS at temperatures of 25 °C, 37 °C and 50 °C shown in Figure 4(c) till 1 % strain. The experiments were performed using the ARES G2 Rheometer and the cone and plate geometry (40 mm diameter and 0.04 radian cone angle). Three repetitions were performed for each experimental result reported. Konale and co-workers (Konale et al., 2023) established that the crossover frequency in small strain frequency sweep experiments is proportional to the backward reaction rate parameter (k_{ns}) for the reversible reaction involving subchain dissociation in (4.23). Assuming Arrhenius temperature dependence of k_{ns} , the activation energy for the backward reaction, i.e., subchain dissociation can be obtained by fitting to the crossover frequencies in Figure 4(c) as 24 kJ/mol, which is in the same order of magnitude as the subchain dissociation energy (15 kJ/mol). This same order of magnitude similarity between activation energy and subchain dissociation energy is reasonable considering (a) the relative simplicity of the chemical reaction under consideration - only one type of bond (B:O coordinate-bond) is involved and (b) the assumptions made during the estimation analyses. Further, the subchain dissociation energy value lies in the range of weak, non-covalent bond energies reported in the literature (Burley and Petsko, 1988, Wang et al., 2017, Buaksuntear et al., 2022).

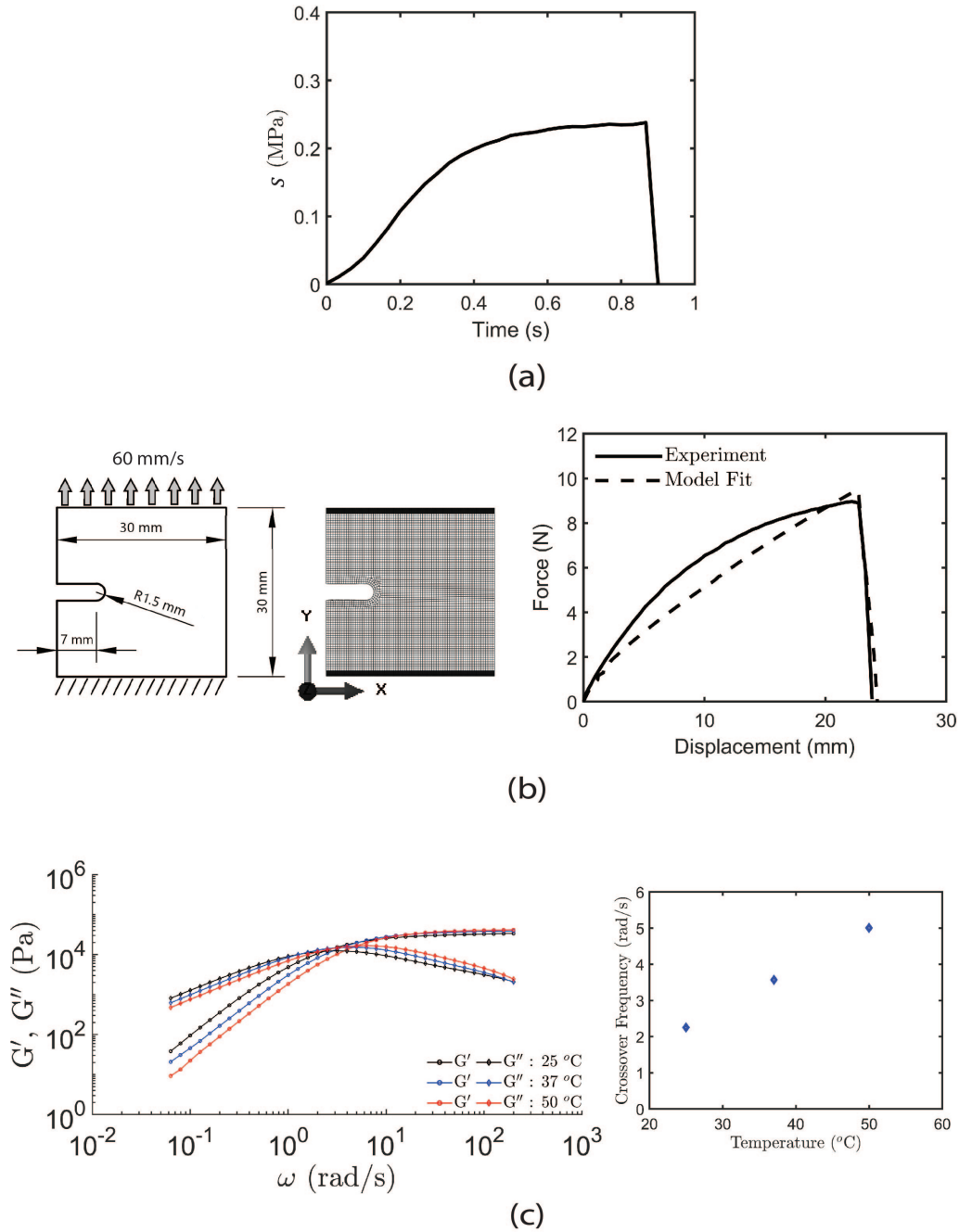


Figure 4: (a) Engineering stress (s) vs. time curve for the uniaxial tension experiment on PBS. The gauge section of the specimen undergoes stretching at an engineering strain rate of 4 s^{-1} . (b) Schematic for notched PBS tension experiment. The specimen has a thickness of 3.2 mm and was subjected to a loading speed of 60 mm/s. Finite element mesh used for simulation. Fit of the model (dashed lines) to the experimental extension force-displacement curve. (c) Oscillatory shear response of PBS (1% shear strain) at 25 °C, 37 °C and 50 °C. Crossover frequency vs. temperature plot for PBS.

6. Model predictions for fracture in a variety of soft polymers

The model is applied to predict fracture in select soft polymers - a permanently crosslinked rubber [ethylene propylene diene monomer (EPDM)], PBS, and dynamically crosslinked EPS25 vitrimer. Three independent experiments were performed on PBS with different specimen geometries and loading configurations subjected to a range of stretching speeds. *The previously calibrated model parameters for PBS obtained using the notched tension experiment in Figure 4(b) were kept fixed for independent validations. This allowed for an independent true assessment of the model’s predictive capabilities for the three validation experiments on PBS.* Experimental data reported in (Benvidi et al., 2019) and (Shen et al., 2021) is used to test the predictive abilities of the proposed model for EPDM rubber and EPS25 vitrimer, respectively. Based on the experimental material response, intermolecular resistance (mechanism *A*) is neglected for modeling the deformation of EPDM rubber and EPS25 vitrimer in (Benvidi et al., 2019, Shen et al., 2021), i.e., $\psi_o^{(A)} = 0$ and $\psi_o = \psi_o^{(B)}$. For the network resistance (mechanism *B*), the free energy density functions with the dynamic crosslink formulation for the hyperelastic function part were the same as used in (Benvidi et al., 2019, Shen et al., 2021) for EPDM rubber, EPS25 vitrimer. This also allowed us to test the dynamic crosslink formulation’s predictive capabilities for different hyperelastic free energy density base functions. Deformation-related material parameters for EPDM and EPS25 vitrimer are taken from (Benvidi et al., 2019, Shen et al., 2021).

6.1. PBS: Single edge notch

A U-shaped edge notch with depth and radius of 18.5 mm and 3 mm, respectively was created equidistant from the gripping fixtures in the gauge section with dimensions 30 ± 2 mm x 30 ± 2 mm x 3.2 ± 1 mm. This is a much deeper notch than what was used for calibration. The specimen geometry for the experiment schematic shown in Figure 5(a) was stretched at 60 mm/s. The finite element mesh (31,892 C3D8R elements) used for simulation is shown in Figure 5(a). The specimen was stretched until failure. Good agreement between the prediction from simulation and experimental result for the extension force can be seen in Figure 5(b). Specimen geometry changes at different displacement levels from the experiment and simulation are shown in Figure 5(c), which also shows very good agreement between the experimental and simulation results. Particularly the trumpet fracture profile (formation of second local notch ahead of the original blunted notch) observed experimentally in Figure 5(c)[iv] is predicted by the model. Also, the model correctly predicts the transition from rupture with low extensibility at a fast loading rate (60 mm/s) to high extensibility at a slow loading rate (6 mm/s) as shown in Figure 5(c). The high extensibility at the relatively

slower loading speed of 6 mm/s is due to ψ_o^+ , $\psi_o^{(B)}$ at the notch center not being able to exceed ψ_{cr}^+ and $\psi_{cr}^{(B)}$, respectively.

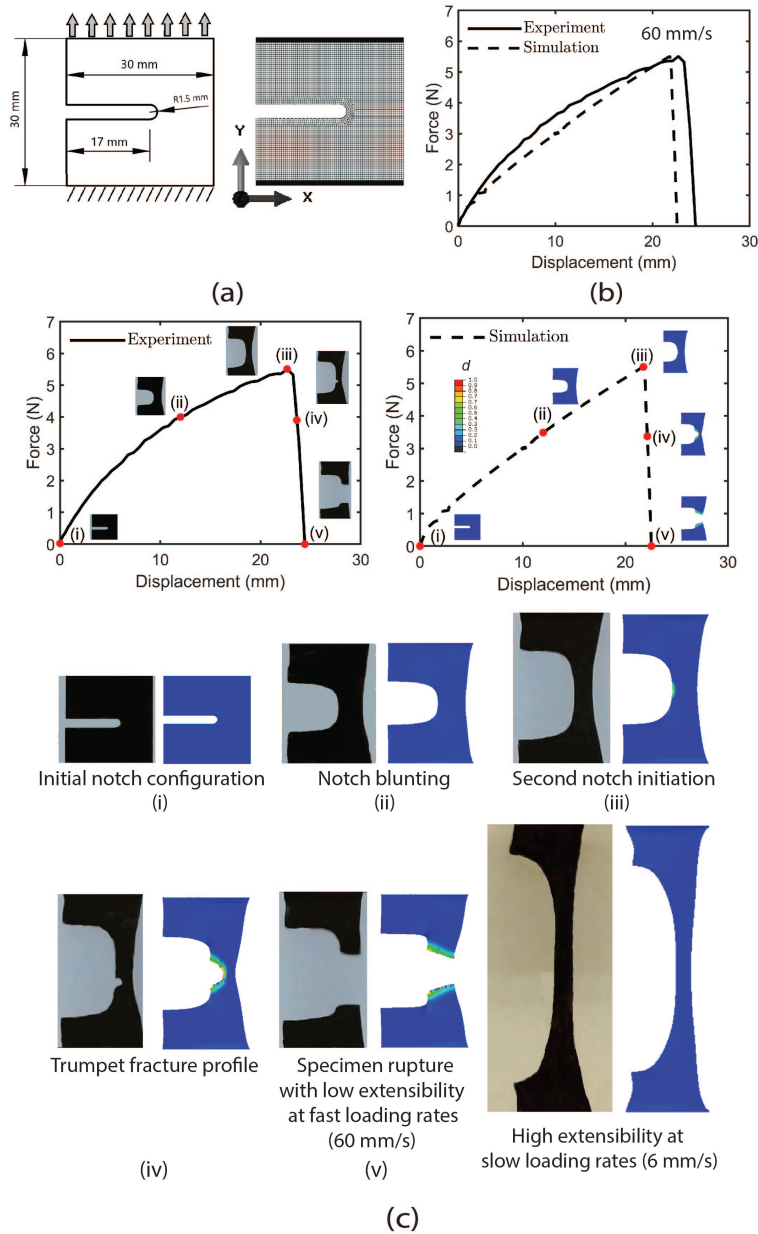


Figure 5: (a) Edge notch PBS stretch experiment schematic. Finite element mesh used for simulation. (b) Good agreement between the numerically predicted force-displacement curve and the experimental result for 60 mm/s loading speed. (c) Specimen shapes at different levels of stretch from experiment (left) and simulation (right) show good agreement for the 60 mm/s stretching speed. The model predicts the experimentally observed trumpet fracture profile. Also, the model predicts the transition from rupture with low extensibility at a fast loading rate (60 mm/s) to high extensibility at a slow loading rate (6 mm/s). Elements with $d > 0.95$ are hidden and the experimental specimen was colored for visualization.

6.2. PBS: Center notch

To validate the model predictions for PBS in a scenario involving a different notch geometry (same gauge section dimensions and boundary conditions as the single edge notch geometry), a 10 mm x 3 mm slot was created at the center of the gauge section as shown in Figure 6(a). Further, relatively low loading speeds of 2 mm/s and 6 mm/s were used for this geometry. The finite element mesh used for the simulations is shown in Figure 6(b). One-quarter of the specimen (25,832 C3D8R elements) was simulated with appropriate boundary conditions considering the symmetries of the problem. For these relatively slower speeds, the experimental results exhibit necking instability in the form of the non-positive slope of force-displacement curves after a certain level of displacement. This can be attributed to significant network reconfiguration occurring over these long timescales (relative to the B:O coordinate bond dynamic crosslink macroscopic relaxation timescale) as a result of dynamic crosslink relaxation and reformation. Model predictions for the force-displacement curves, particularly the displacement levels for the onset of necking instability agree well with the experimental results as seen in Figure 6(c). Fracture doesn't occur for these slow loading speeds which can be attributed to ψ_o^+ , $\psi_o^{(B)}$ not being able to exceed ψ_{cr}^+ and $\psi_{cr}^{(B)}$, respectively at the notch center. The specimens exhibited high extensibility in the experiments as shown in Figure 6(d) through a comparison between the undeformed and deformed shapes.

6.3. PBS: Stretching using inserts

The fracture model is now applied to a different loading configuration. The PBS specimen has two 5 mm diameter symmetric holes in the gauge section (same dimensions as the single edge notch geometry) as shown in Figure 7(a). 3D-printed hard plastic (PLA) inserts of the same diameter placed in the holes are then used to stretch the specimen. The bottom insert is held fixed while the top insert is displaced at 60 mm/s. Figure 7(a) shows the experiment schematic. The finite element mesh used for the simulation is shown in Figure 7(b). One-quarter of the specimen (29,016 C3D8R elements) was simulated with appropriate boundary conditions considering the symmetries of the problem. The specimen was stretched until failure. The inserts were modeled as rigid analytical surfaces. Contact between the inserts and the specimen was assumed to be frictionless as the interfaces were lubricated in the experiments. Model prediction for the extension force agrees well with the experimental result, as shown in Figure 7(c).

6.4. Fracture response considering viscous effects

We performed simulations where the viscous effects in the input material were removed (by suitably prescribing the material parameter values) to study the role of viscosity in the physical fracture phenomenon. These enabled qualitative model predictions for fracture

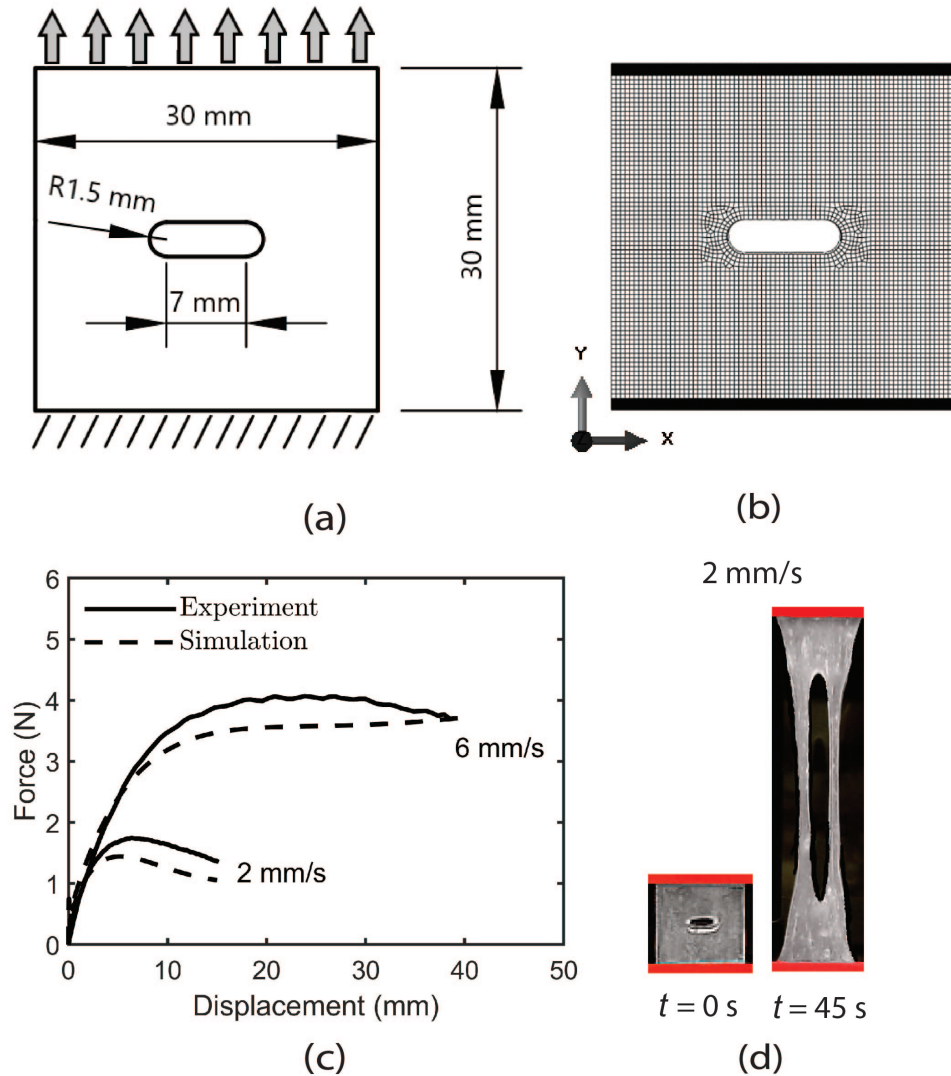


Figure 6: (a) Center notch PBS stretch experiment schematic. (b) Finite element mesh for the simulations. Quarter symmetry with appropriate symmetry boundary conditions was used in the simulations, but for clarity, complete geometry with mesh is shown. (c) Good agreement between the model predictions and the experimental results can be seen for the two loading speeds of 2 mm/s and 6 mm/s. Necking instability seen in the experimental results is predicted by the model and fracture doesn't occur at these slower speeds. (d) High extensibility is shown through the comparison of specimen shapes at $t = 0$ s and $t = 45$ s for a 2 mm/s loading speed.

profiles as the material varies from a viscous soft polymer to an elastomer. The geometry, loading schematic, and finite element mesh for the notched tension test in Figure 4(b) were considered with a stretching speed of 60 mm/s. ζ , which determines the timescale for damage growth was set equal to 3 kPa.s. All other material parameters for PBS are left unchanged

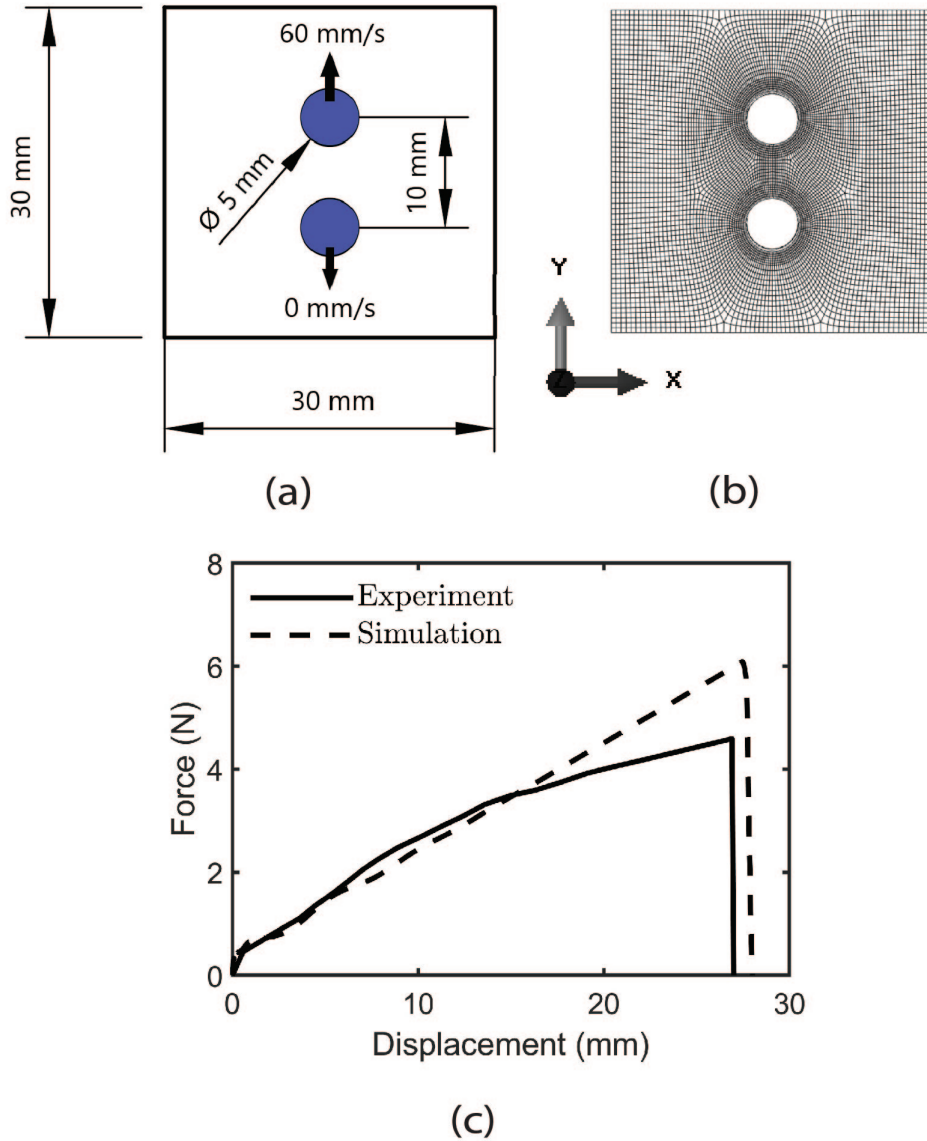


Figure 7: (a) PBS specimen geometry and experiment schematic. The blue regions denote the inserts. The specimen has a thickness of 3.2 mm and the top insert was displaced at a speed of 60 mm/s. (b) Finite element mesh used for the simulation. A quarter of the block is considered due to the symmetries of the problem with appropriate boundary conditions. For clarity, complete geometry with mesh is shown. (c) The model prediction for the extension force agrees well with the experimental result.

except G , k_{ns} and k_s . We removed viscous effects by setting $G = 0$ (removing the elastic-viscoplastic A branch/micromechanism) and $k_{ns} = k_s = 0$ (this provides a model representing permanently crosslinked material) to simulate a hyperelastic material. The computationally obtained fracture profiles in Figure 8 transition correctly from the experimentally observed trumpet profile in viscous soft polymers (de Gennes, 1996, Hui et al., 2022, Shen et al., 2021)

to single parabola-like profile in elastomers (Qi et al., 2019, Shrivastava et al., 2023). The model can predict the significantly varying important physical phenomena observed during the fracture of soft polymers.

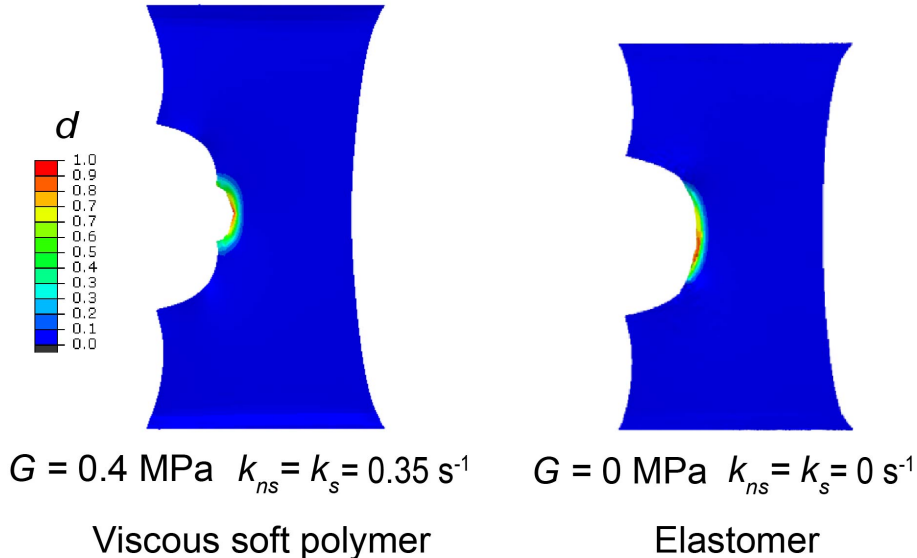
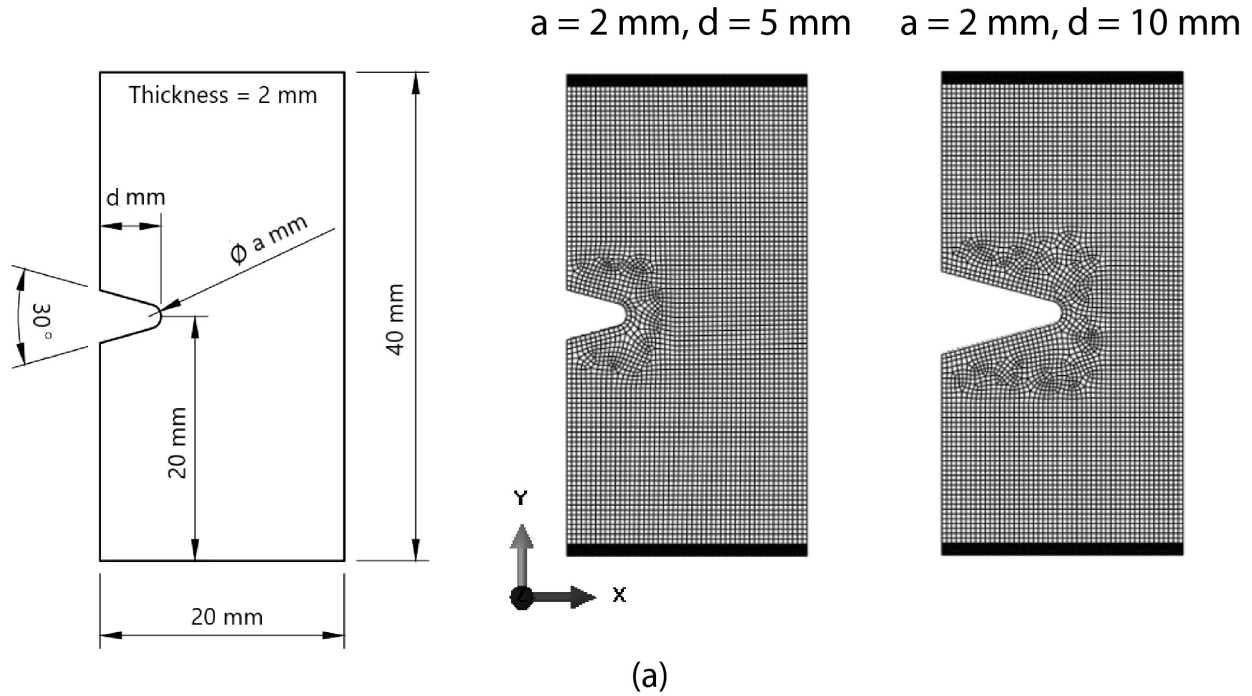


Figure 8: Notch profiles for single notch specimen stretching simulations showing experimentally observed trumpet profile for a viscous soft polymer (PBS) and a single parabola-like profile when viscous effects were removed in the model to simulate elastomeric material response. The profiles are shown just before complete failure. Elements with $d > 0.95$ are hidden for visualization.

6.5. EPDM elastomer with V notch

Benvidi and co-workers (Benvidi et al., 2019) performed tension tests on V-notched EPDM rubber to demonstrate the efficacy of the average strain energy density criterion for fracture analysis of hyperelastic materials. We test our fracture model’s ability to capture the experimental data reported in (Benvidi et al., 2019). The two notch configurations from (Benvidi et al., 2019) shown in Figure 9(a) were applied in finite element simulations for our model’s verification. A total of 20,265 and 20,019 C3D8R elements were used in the finite element meshes for notch diameter $a=2$ mm, notch depth $d=5$ mm and $a=2$ mm, $d=10$ mm cases respectively as shown in Figure 9(a). Due to the assumed hyperelastic nature of EPDM in (Benvidi et al., 2019), $W_{cr} = \psi_{cr}^+ = \psi_{cr}^{(B)}$. The Ogden free energy density function was used in (Benvidi et al., 2019) to model the large deformation response of the EPDM elastomer. Instead of the eight-chain free energy density function with the dynamic crosslink formulation for Mechanism B , the Ogden function is used with the same dynamic crosslink formulation for our fracture modeling framework. We set $G=0$ MPa, $k_{ns} = k_s=0 \text{ s}^{-1}$ in our model and used the deformation-related material parameters from (Benvidi et al., 2019). As

the force-displacement curves for the V notched tests are not presented in (Benvidi et al., 2019), it was assumed that rupture occurs instantly when $\psi_o^+ = \psi_o^{(B)} = \psi_{cr}^+$ at the notch center. Independent prediction for the displacement at which rupture occurs for the a=2 mm and d=10 mm notch geometry agrees well with the experimental result as shown in Figure 9(b).



Notch depth d (mm)	Experimental rupture displacement (mm) data from Benvidi et al. (2019)	Model prediction (mm)
5	28.26	Used for ψ_{cr}^+ calibration
10	23.07	22.55 (independent prediction)

(b)

Figure 9: (a) V-notched specimen geometry for EPDM rubber used in (Benvidi et al., 2019). Finite element meshes used for simulations. (b) Experimental data for a=2 mm, d=5 mm from (Benvidi et al., 2019) was used for $\psi_{cr}^+ = \psi_{cr}^{(B)} = W_{cr}$ calibration. Independent model prediction for the rupture displacement for a=2 mm, d=10 mm notch geometry shows good agreement with the experimental result in (Benvidi et al., 2019).

6.6. EPS25 vitrimer: Notched pure shear

To test the model predictions for a different dynamically crosslinked soft polymer and a loading mode other than tension, we utilize the data reported by Shen and co-workers (Shen et al., 2021) for the fracture of EPS25 vitrimer. Pure shear tests over a range of loading speeds were performed on EPS25 vitrimer specimens with sharp single edge notches in (Shen et al., 2021). The specimen geometry is shown in Figure 10(a). Crack extension vs stretch ratio (λ) experimental data for the two loading speeds reported in (Shen et al., 2021) is shown in 10(c). The authors observed a transition from high extensibility, i.e., no crack propagation (0.0225 mm/s) to fracture (0.09 mm/s) with increasing loading rates as shown in Figure 10(c). The transient network theory with the neo-Hookean free energy density function is used by the authors to model the large deformation response of EPS25 vitrimer. We used the neo-Hookean function for mechanism B with our same dynamic crosslink formulation. G is set equal to 0 MPa in our model, and the deformation-associated material parameters from (Shen et al., 2021) are used. The authors created a sharp notch in the specimens using a blade. As the exact radius of the notch is not specified in (Shen et al., 2021), we assumed a very sharp notch radius of 100 μm . With the aim of modeling the initiation of crack propagation, only a VUMAT was used. A total of 28,716 C3D8 (three-dimensional, full integration) stress elements were used in the finite element mesh for the problem as shown in 10(b). $\psi_{cr}^+ = \psi_{cr}^{(B)}$, W_{cr} were evaluated as the values of $\psi_o^+ = \psi_o^{(B)}$, W at the notch center at the time instant corresponding to the initiation of crack propagation for the 0.09 mm/s loading speed. Model predictions for ψ_o^+ at the notch center vs. λ curves for the two loading speeds are shown in 10(d). The model predicts no crack propagation for the relatively slow 0.0225 mm/s loading speed due to ψ_o^+ at the notch center not being able to exceed ψ_{cr}^+ as seen in Figure 10(d). This agrees with the experimental observation from (Shen et al., 2021) in Figure 10(c).

7. Conclusions

Current fracture toughness measures are non-unique for rate-dependent soft polymers for varying loading profiles and specimen geometries. We propose that a critical value of stress work W_{cr} can quantify the fracture resistance of soft polymers. W_{cr} can be interpreted as the total energy per unit referential volume associated with the complete failure of a material point under a loading mode subjected to sufficiently fast loading rates for damage initiation. Simple experiments involving homogeneous deformations can be used to evaluate W_{cr} without the need for constitutive models. We show W_{cr} to be approximately constant with strain rate for two rate-dependent soft polymers and loading modes for an elastomer. A model is developed to predict damage initiation, damage growth, and complete failure

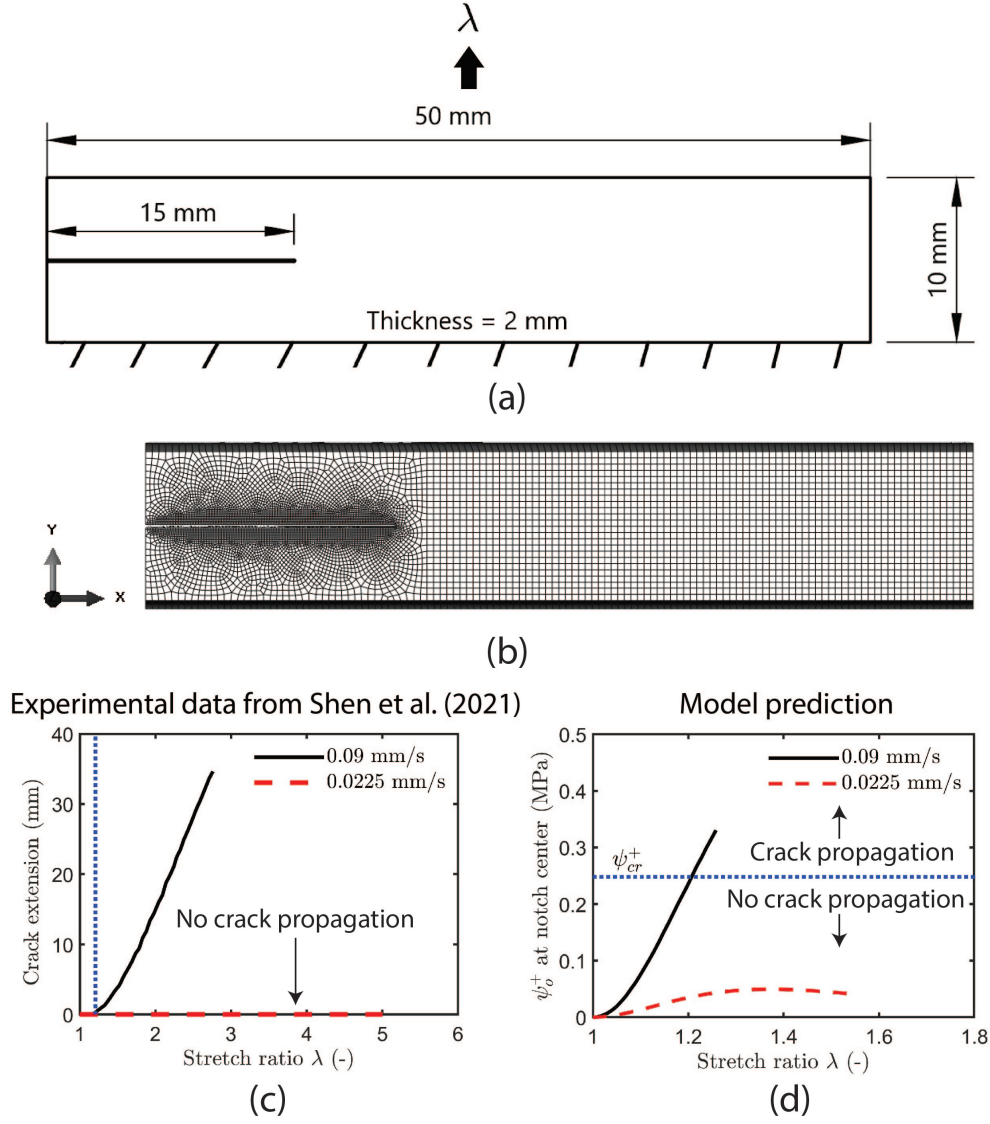


Figure 10: (a) Specimen geometry for EPS25 vitrimer pure shear tests with sharp single edge notches from (Shen et al., 2021). (b) Finite element mesh for simulations. (c) Crack extension vs. stretch ratio (λ) experimental data from (Shen et al., 2021) for the loading speeds of 0.09 mm/s and 0.0225 mm/s. There is no crack propagation for 0.0225 mm/s loading speed. $\psi_{cr}^+ = \psi_{cr}^{(B)}$ and W_{cr} were calibrated using the λ at initiation of crack propagation for 0.09 mm/s speed. (d) Model predictions for ψ_o^+ at the notch center vs λ curves for the two loading speeds. The model predicts no crack propagation for 0.0225 mm/s speed due to ψ_o^+ at the notch center not being able to exceed ψ_{cr}^+ . This agrees with the experimental observation in (Shen et al., 2021).

in soft polymers based on the gradient damage framework. W_{cr} for Polyborosiloxane, a dynamic, reversibly crosslinked soft polymer, was evaluated using simple tension tests. The energetic contribution to W_{cr} was used as a criterion for damage initiation in the model. This resulted in the successful prediction of Polyborosiloxane's fracture in independent ex-

periments involving different specimen geometries and loading conditions. We were able to approximate the energy density for fracture-related microstructural processes using the physical understanding of macroscopic model parameters. The fracture model's predictive capabilities were also verified on an elastomer and another viscous soft polymer, for which experimental data was available in the literature. A transition in fracture profile from trumpet to single parabola-like was observed in the model predictions as the polymer viscous effects were removed. This is consistent with experimental observations, demonstrating the model's ability to predict the significantly varying physical phenomena observed during the fracture of soft polymers.

Author Contributions

Aditya Konale: Investigation, Methodology, Formal analysis, Data curation, Software, Visualization, Writing – original draft preparation, review & editing. **Vikas Srivastava:** Conceptualization, Investigation, Methodology, Supervision, Funding acquisition, Writing – original draft preparation, review & editing.

Acknowledgments

The authors would like to acknowledge the support from the Office of Naval Research (ONR), USA to V. Srivastava under grant numbers N00014-21-1-2815 and N00014-21-1-2670. The authors thank Dr. James LeBlanc from the Naval Underwater Warfare Center for supporting the research work.

Declaration of Interest

The authors declare no competing interests.

References

- D. Ahmad, S. K. Sahu, and K. Patra. Fracture toughness, hysteresis and stretchability of dielectric elastomers under equibiaxial and biaxial loading. *Polymer Testing*, 79:106038, 2019. ISSN 0142-9418. doi: <https://doi.org/10.1016/j.polymertesting.2019.106038>.
- N. M. Ames, V. Srivastava, S. A. Chester, and L. Anand. A thermo-mechanically coupled theory for large deformations of amorphous polymers. part ii: Applications. *International Journal of Plasticity*, 25(8):1495–1539, 2009. ISSN 0749-6419. doi: <https://doi.org/10.1016/j.ijplas.2008.11.005>.

- M. Amjadi, Y. J. Yoon, and I. Park. Ultra-stretchable and skin-mountable strain sensors using carbon nanotubes–ecoflex nanocomposites. *Nanotechnology*, 26(37):375501, aug 2015. doi: 10.1088/0957-4484/26/37/375501.
- H. Amor, J.-J. Marigo, and C. Maurini. Regularized formulation of the variational brittle fracture with unilateral contact: Numerical experiments. *Journal of the Mechanics and Physics of Solids*, 57(8):1209–1229, 2009. ISSN 0022-5096. doi: <https://doi.org/10.1016/j.jmps.2009.04.011>.
- L. Anand, N. M. Ames, V. Srivastava, and S. A. Chester. A thermo-mechanically coupled theory for large deformations of amorphous polymers. part i: Formulation. *International Journal of Plasticity*, 25(8):1474–1494, 2009. ISSN 0749-6419. doi: <https://doi.org/10.1016/j.ijplas.2008.11.004>.
- L. Anand, Y. Mao, and B. Talamini. On modeling fracture of ferritic steels due to hydrogen embrittlement. *Journal of the Mechanics and Physics of Solids*, 122:280–314, 2019. ISSN 0022-5096. doi: <https://doi.org/10.1016/j.jmps.2018.09.012>.
- E. M. Arruda and M. C. Boyce. A three-dimensional constitutive model for the large stretch behavior of rubber elastic materials. *Journal of the Mechanics and Physics of Solids*, 41(2):389–412, 1993. ISSN 0022-5096. doi: [https://doi.org/10.1016/0022-5096\(93\)90013-6](https://doi.org/10.1016/0022-5096(93)90013-6).
- Y. Bai, N. J. Kaiser, K. L. Coulombe, and V. Srivastava. A continuum model and simulations for large deformation of anisotropic fiber–matrix composites for cardiac tissue engineering. *Journal of the Mechanical Behavior of Biomedical Materials*, 121:104627, 9 2021. ISSN 17516161. doi: <https://doi.org/10.1016/j.jmbbm.2021.104627>.
- A. H. Benvidi, M. R. Ayatollahi, and M. Heydari-Meybodi. Fracture analysis of rounded-tip v-notched components made of rubber-like materials using averaged strain energy density criterion. *Procedia Structural Integrity*, 21:12–20, 2019. ISSN 2452-3216. doi: <https://doi.org/10.1016/j.prostr.2019.12.081>. 1st International Workshop on Plasticity, Damage and Fracture of Engineering Materials, IWPDF 2019, 22-23 August 2019, Ankara, Turkey.
- J. Bergström and M. Boyce. Constitutive modeling of the large strain time-dependent behavior of elastomers. *Journal of the Mechanics and Physics of Solids*, 46(5):931–954, 1998. ISSN 0022-5096. doi: [https://doi.org/10.1016/S0022-5096\(97\)00075-6](https://doi.org/10.1016/S0022-5096(97)00075-6).

- M. Boyce, G. Weber, and D. Parks. On the kinematics of finite strain plasticity. *Journal of the Mechanics and Physics of Solids*, 37(5):647–665, 1989. ISSN 0022-5096. doi: [https://doi.org/10.1016/0022-5096\(89\)90033-1](https://doi.org/10.1016/0022-5096(89)90033-1).
- M. C. Boyce, D. M. Parks, and A. S. Argon. Large inelastic deformation of glassy polymers. part i: rate dependent constitutive model. *Mechanics of Materials*, 7(1):15–33, 1988. ISSN 0167-6636. doi: [https://doi.org/10.1016/0167-6636\(88\)90003-8](https://doi.org/10.1016/0167-6636(88)90003-8).
- W. Brostow, H. E. Hagg Lobland, and S. Khoja. Brittleness and toughness of polymers and other materials. *Materials Letters*, 159:478–480, 2015. ISSN 0167-577X. doi: <https://doi.org/10.1016/j.matlet.2015.07.047>.
- E. N. Brown, N. R. Sottos, and S. R. White. Fracture testing of a self-healing polymer composite. *Experimental Mechanics*, 42(4):372–379, 2002. doi: [10.1007/BF02412141](https://doi.org/10.1007/BF02412141).
- K. Buaksuntear, P. Limarun, S. Suethao, and W. Smitthipong. Non-covalent interaction on the self-healing of mechanical properties in supramolecular polymers. *International Journal of Molecular Sciences*, 23(13), 2022. ISSN 1422-0067. doi: [10.3390/ijms23136902](https://doi.org/10.3390/ijms23136902).
- B. Budiansky and J. R. Rice. Conservation Laws and Energy-Release Rates. *Journal of Applied Mechanics*, 40(1):201–203, 03 1973. ISSN 0021-8936. doi: [10.1115/1.3422926](https://doi.org/10.1115/1.3422926).
- F. Burla, S. Dussi, C. Martinez-Torres, J. Tauber, J. van der Gucht, and G. H. Koenderink. Connectivity and plasticity determine collagen network fracture. *Proceedings of the National Academy of Sciences*, 117(15):8326–8334, 2020. doi: <https://doi.org/10.1073/pnas.1920062117>.
- S. Burley and G. Petsko. Weakly polar interactions in proteins. *Advances in Protein Chemistry*, 39:125–189, 1988. ISSN 0065-3233. doi: [https://doi.org/10.1016/S0065-3233\(08\)60376-9](https://doi.org/10.1016/S0065-3233(08)60376-9).
- C. Chen, Z. Wang, and Z. Suo. Flaw sensitivity of highly stretchable materials. *Extreme Mechanics Letters*, 10:50–57, 2017. ISSN 2352-4316. doi: <https://doi.org/10.1016/j.eml.2016.10.002>. Filling Gaps in Material Property Space: IUTAM Symposium.
- S. Chen and K. Ravi-Chandar. Rate-dependent fracture behavior of gelatin-based hydrogels. *International Journal of Fracture*, 243(2):185–202, Oct 2023. doi: [10.1007/s10704-023-00738-3](https://doi.org/10.1007/s10704-023-00738-3).
- C. Creton. 50th anniversary perspective: Networks and gels: Soft but dynamic and tough. *Macromolecules*, 50(21):8297–8316, 2017. doi: [10.1021/acs.macromol.7b01698](https://doi.org/10.1021/acs.macromol.7b01698).

- P. G. de Gennes. Soft adhesives. *Langmuir*, 12(19):4497–4500, 1996. doi: 10.1021/la950886y.
- R. de Rooij and E. Kuhl. Constitutive modeling of brain tissue: Current perspectives. *Applied Mechanics Reviews*, 68:010801, 2016.
- A. Drozdov and J. deC. Christiansen. Tension–compression asymmetry in the mechanical response of hydrogels. *Journal of the Mechanical Behavior of Biomedical Materials*, 110:103851, 2020. ISSN 1751-6161. doi: <https://doi.org/10.1016/j.jmbbm.2020.103851>.
- T. T. Duncan, J. M. Sarapas, A. P. Defante, K. L. Beers, and E. P. Chan. Cutting to measure the elasticity and fracture of soft gels. *Soft Matter*, 16:8826–8831, 2020. doi: 10.1039/D0SM01174F.
- S. Fakhouri, S. B. Hutchens, and A. J. Crosby. Puncture mechanics of soft solids. *Soft Matter*, 11:4723–4730, 2015. doi: 10.1039/C5SM00230C.
- P. Germain. The method of virtual power in continuum mechanics. part 2: Microstructure. *SIAM Journal on Applied Mathematics*, 25(3):556–575, 1973. doi: 10.1137/0125053.
- J. Guo, M. Liu, A. T. Zehnder, J. Zhao, T. Narita, C. Creton, and C.-Y. Hui. Fracture mechanics of a self-healing hydrogel with covalent and physical crosslinks: A numerical study. *Journal of the Mechanics and Physics of Solids*, 120:79–95, 2018. ISSN 0022-5096. doi: <https://doi.org/10.1016/j.jmps.2018.03.009>. Special issue in honor of Ares J. Rosakis on the occasion of his 60th birthday.
- J. Guo, C.-Y. Hui, M. Liu, and A. T. Zehnder. The stress field near the tip of a plane stress crack in a gel consisting of chemical and physical cross-links. *Proceedings of the Royal Society A: Mathematical, Physical and Engineering Sciences*, 475(2227):20180863, 2019. doi: 10.1098/rspa.2018.0863.
- M. E. Gurtin. Generalized ginzburg-landau and cahn-hilliard equations based on a microforce balance. *Physica D: Nonlinear Phenomena*, 92(3):178–192, 1996. ISSN 0167-2789. doi: [https://doi.org/10.1016/0167-2789\(95\)00173-5](https://doi.org/10.1016/0167-2789(95)00173-5).
- M. E. Gurtin. A gradient theory of single-crystal viscoplasticity that accounts for geometrically necessary dislocations. *Journal of the Mechanics and Physics of Solids*, 50(1):5–32, 2002. ISSN 0022-5096. doi: [https://doi.org/10.1016/S0022-5096\(01\)00104-1](https://doi.org/10.1016/S0022-5096(01)00104-1).
- M. E. Gurtin, E. Fried, and L. Anand. *The mechanics and thermodynamics of continua*. Cambridge university press, 2010.

- O. Gültekin, H. Dal, and G. A. Holzapfel. A phase-field approach to model fracture of arterial walls: Theory and finite element analysis. *Computer Methods in Applied Mechanics and Engineering*, 312:542–566, 2016. ISSN 0045-7825. doi: <https://doi.org/10.1016/j.cma.2016.04.007>. Phase Field Approaches to Fracture.
- L. Hai, P. Wriggers, Y. jie Huang, H. Zhang, and S. lang Xu. Dynamic fracture investigation of concrete by a rate-dependent explicit phase field model integrating viscoelasticity and micro-viscosity. *Computer Methods in Applied Mechanics and Engineering*, 418:116540, 2024. ISSN 0045-7825. doi: <https://doi.org/10.1016/j.cma.2023.116540>.
- P. Hesammokri, H. Yu, and P. Isaksson. An extended hydrostatic–deviatoric strain energy density decomposition for phase-field fracture theories. *International Journal of Solids and Structures*, 262-263:112080, 2023. ISSN 0020-7683. doi: <https://doi.org/10.1016/j.ijsolstr.2022.112080>.
- T. Hu, J. Guilleminot, and J. E. Dolbow. A phase-field model of fracture with frictionless contact and random fracture properties: Application to thin-film fracture and soil desiccation. *Computer Methods in Applied Mechanics and Engineering*, 368:113106, 2020. ISSN 0045-7825. doi: <https://doi.org/10.1016/j.cma.2020.113106>.
- X. Hu, J. Zhou, W. F. M. Daniel, M. Vatankhah-Varnoosfaderani, A. V. Dobrynin, and S. S. Sheiko. Dynamics of dual networks: Strain rate and temperature effects in hydrogels with reversible h-bonds. *Macromolecules*, 50(2):652–659, 2017. doi: 10.1021/acs.macromol.6b02422.
- X. Huang, B. Li, W. Hong, Y.-P. Cao, and X.-Q. Feng. Effects of tension–compression asymmetry on the surface wrinkling of film–substrate systems. *Journal of the Mechanics and Physics of Solids*, 94:88–104, 2016. ISSN 0022-5096. doi: <https://doi.org/10.1016/j.jmps.2016.04.014>.
- N. Huebsch, C. J. Kearney, X. Zhao, J. Kim, C. A. Cezar, Z. Suo, and D. J. Mooney. Ultrasound-triggered disruption and self-healing of reversibly cross-linked hydrogels for drug delivery and enhanced chemotherapy. *Proceedings of the National Academy of Sciences*, 111(27):9762–9767, 2014. doi: <https://doi.org/10.1073/pnas.1405469111>.
- C. Y. Hui, J. Guo, M. Liu, and A. Zehnder. Finite strain theory of a mode iii crack in a rate dependent gel consisting of chemical and physical cross-links. *International Journal of Fracture*, 215(1):77–89, Jan 2019. ISSN 1573-2673. doi: 10.1007/s10704-018-00335-9.

- C.-Y. Hui, B. Zhu, and R. Long. Steady state crack growth in viscoelastic solids: A comparative study. *Journal of the Mechanics and Physics of Solids*, 159:104748, 2022. ISSN 0022-5096. doi: <https://doi.org/10.1016/j.jmps.2021.104748>.
- C. Imaoka, T. Nakajima, T. Indei, M. Iwata, W. Hong, A. Marcellan, and J. P. Gong. Inverse mechanical-swelling coupling of a highly deformed double-network gel. *Science Advances*, 9(19):eabp8351, 2023. doi: [10.1126/sciadv.abp8351](https://doi.org/10.1126/sciadv.abp8351).
- A. International. *ASTM D638-14, Standard Test Method for Tensile Properties of Plastics*. ASTM International, 2015.
- M. Jiang, Z. T. Lawson, V. Erel, S. Pervere, T. Nan, A. B. Robbins, A. D. Feed, and M. R. Moreno. Clamping soft biologic tissues for uniaxial tensile testing: A brief survey of current methods and development of a novel clamping mechanism. *J Mech Behav Biomed Mater*, 103:103503, Nov. 2019.
- Y. M. Jihai Yuan and C. Chen. Multiple-phase-field modeling for fracture of composite materials. *Mechanics of Advanced Materials and Structures*, 29(28):7476–7490, 2022. doi: [10.1080/15376494.2021.2000081](https://doi.org/10.1080/15376494.2021.2000081).
- Y.-L. Kang, Z.-F. Zhang, H.-W. Wang, and Q.-H. Qin. Experimental investigations of the effect of thickness on fracture toughness of metallic foils. *Materials Science and Engineering: A*, 394(1):312–319, 2005. ISSN 0921-5093. doi: <https://doi.org/10.1016/j.msea.2004.11.044>.
- J. Kim, Y. Kim, H. Shin, and W.-R. Yu. Mechanical modeling of strain rate-dependent behavior of shear-stiffening gel. *International Journal of Mechanics and Materials in Design*, Oct 2022. doi: <https://doi.org/10.1007/s10999-022-09618-5>.
- D. R. King. Macroscale double networks: highly dissipative soft composites. *Polymer Journal*, 54(8):943–955, Aug 2022. ISSN 1349-0540. doi: [10.1038/s41428-022-00646-8](https://doi.org/10.1038/s41428-022-00646-8).
- A. Konale, Z. Ahmed, P. Wanchoo, and V. Srivastava. A large deformation model for quasi-static to high strain rate response of a rate-stiffening soft polymer. *International Journal of Plasticity*, 168:103701, 2023. ISSN 0749-6419. doi: <https://doi.org/10.1016/j.ijplas.2023.103701>.
- S. Konica and T. Sain. A reaction-driven evolving network theory coupled with phase-field fracture to model polymer oxidative aging. *Journal of the Mechanics and Physics of Solids*, 150:104347, 2021. ISSN 0022-5096. doi: <https://doi.org/10.1016/j.jmps.2021.104347>.

- S. Konica, B. W. Sheldon, and V. Srivastava. Role of coupled electrochemistry and stress on the li-anode instability: A continuum approach, 2024.
- M. Kothari, S. Niu, and V. Srivastava. A thermo-mechanically coupled finite strain model for phase-transitioning austenitic steels in ambient to cryogenic temperature range. *Journal of the Mechanics and Physics of Solids*, 133:103729, 2019. ISSN 0022-5096. doi: <https://doi.org/10.1016/j.jmps.2019.103729>.
- E. Kröner. Allgemeine kontinuumstheorie der versetzungen und eigenspannungen. *Archive for Rational Mechanics and Analysis*, 4(1):273–334, Jan 1959. ISSN 1432-0673. doi: <https://doi.org/10.1007/BF00281393>.
- A. Kurkin, V. Lipik, K. B. L. Tan, G. L. Seah, X. Zhang, and A. I. Y. Tok. Correlations between precursor molecular weight and dynamic mechanical properties of polyborosiloxane (pbs). *Macromolecular Materials and Engineering*, 306(11):2100360, 2021. doi: <https://doi.org/10.1002/mame.202100360>.
- J.-C. Lai, X.-Y. Jia, D.-P. Wang, Y.-B. Deng, P. Zheng, C.-H. Li, J.-L. Zuo, and Z. Bao. Thermodynamically stable whilst kinetically labile coordination bonds lead to strong and tough self-healing polymers. *Nature Communications*, 10(1):1164, Mar 2019. ISSN 2041-1723. doi: [10.1038/s41467-019-09130-z](https://doi.org/10.1038/s41467-019-09130-z).
- G. J. Lake. Fatigue and Fracture of Elastomers. *Rubber Chemistry and Technology*, 68(3):435–460, 07 1995. ISSN 0035-9475. doi: [10.5254/1.3538750](https://doi.org/10.5254/1.3538750).
- G. J. Lake, A. G. Thomas, and D. Tabor. The strength of highly elastic materials. *Proceedings of the Royal Society of London. Series A. Mathematical and Physical Sciences*, 300(1460):108–119, 1967. doi: [10.1098/rspa.1967.0160](https://doi.org/10.1098/rspa.1967.0160).
- J. LeBlanc, A. Shukla, and Y. D. S. Rajapakse. Dynamic failure of composite materials. *Journal of Dynamic Behavior of Materials*, 4(3):257–257, 2018. doi: [10.1007/s40870-018-0171-5](https://doi.org/10.1007/s40870-018-0171-5).
- J. LeBlanc, P. Cavallaro, J. Torres, D. Ponte, E. Warner, R. Saenger, I. N. Mforsoh, and A. Shukla. Low temperature effects on the mechanical, fracture, and dynamic behavior of carbon and e-glass epoxy laminates. *International Journal of Lightweight Materials and Manufacture*, 3(4):344–356, 2020. ISSN 2588-8404. doi: <https://doi.org/10.1016/j.ijlmm.2020.05.002>.
- E. H. Lee. Elastic-Plastic Deformation at Finite Strains. *Journal of Applied Mechanics*, 36(1):1–6, 03 1969. ISSN 0021-8936. doi: <https://doi.org/10.1115/1.3564580>.

- J. Lee, S. Lee, S. A. Chester, and H. Cho. Finite element implementation of a gradient-damage theory for fracture in elastomeric materials. *International Journal of Solids and Structures*, 279:112309, 2023. ISSN 0020-7683. doi: <https://doi.org/10.1016/j.ijsolstr.2023.112309>.
- J. Lee, J. Lee, S. Yun, S. Kim, H. Lee, S. A. Chester, and H. Cho. Size-dependent fracture in elastomers: experiments and continuum modeling. *arXiv*, 2024. doi: <https://doi.org/10.48550/arXiv.2403.19997>.
- S. P. Lele and L. Anand. A large-deformation strain-gradient theory for isotropic viscoplastic materials. *International Journal of Plasticity*, 25(3):420–453, 2009. ISSN 0749-6419. doi: <https://doi.org/10.1016/j.ijplas.2008.04.003>.
- F. Li, C. Shih, and A. Needleman. A comparison of methods for calculating energy release rates. *Engineering Fracture Mechanics*, 21(2):405–421, 1985. ISSN 0013-7944. doi: [https://doi.org/10.1016/0013-7944\(85\)90029-3](https://doi.org/10.1016/0013-7944(85)90029-3).
- W. Li, H. Nguyen, and Y. Bazilevs. Isogeometric multilayer thin-shell analysis of failure in composite structures with hygrothermal effects. *International Journal of Fracture*, 2024. doi: [10.1007/s10704-024-00808-0](https://doi.org/10.1007/s10704-024-00808-0).
- X. Li, D. Zhang, K. Xiang, and G. Huang. Synthesis of polyborosiloxane and its reversible physical crosslinks. *RSC Adv.*, 4:32894–32901, 2014. doi: <http://dx.doi.org/10.1039/C4RA01877J>.
- B. Liu, C. Du, and Y. Fu. Factors influencing the rheological properties of mrrsp based on the orthogonal experimental design and the impact energy test. *Advances in Materials Science and Engineering*, 2019:2545203, Sep 2019a. ISSN 1687-8434. doi: <https://doi.org/10.1155/2019/2545203>.
- B. Liu, T. Yin, J. Zhu, D. Zhao, H. Yu, and S. Qu. Tough and fatigue-resistant polymer networks by crack tip softening. *Proceedings of the National Academy of Sciences*, 120(6): e2217781120, 2023. doi: <https://doi.org/10.1073/pnas.2217781120>.
- M. Liu, J. Guo, C.-Y. Hui, and A. Zehnder. Crack tip stress based kinetic fracture model of a pva dual-crosslink hydrogel. *Extreme Mechanics Letters*, 29:100457, 2019b. ISSN 2352-4316. doi: <https://doi.org/10.1016/j.eml.2019.100457>.
- R. Long and C.-Y. Hui. Fracture toughness of hydrogels: measurement and interpretation. *Soft Matter*, 12:8069–8086, 2016. doi: [10.1039/C6SM01694D](https://doi.org/10.1039/C6SM01694D).

- R. Long, C.-Y. Hui, J. P. Gong, and E. Bouchbinder. The fracture of highly deformable soft materials: A tale of two length scales. *Annual Review of Condensed Matter Physics*, 12(1):71–94, 2021. doi: 10.1146/annurev-conmatphys-042020-023937.
- F. Luo, T. L. Sun, T. Nakajima, T. Kurokawa, Y. Zhao, A. B. Ihsan, H. L. Guo, X. F. Li, and J. P. Gong. Crack blunting and advancing behaviors of tough and self-healing polyampholyte hydrogel. *Macromolecules*, 47(17):6037–6046, 2014. doi: 10.1021/ma5009447.
- K. A. Mac Donald and G. Ravichandran. Crack propagation and renucleation in soft brittle hydrogels. *International Journal of Fracture*, 222(1):37–52, 2020. doi: 10.1007/s10704-020-00430-w.
- Y.-W. Mai and P. Powell. Essential work of fracture and j-integral measurements for ductile polymers. *Journal of Polymer Science Part B: Polymer Physics*, 29(7):785–793, 1991. doi: <https://doi.org/10.1002/polb.1991.090290702>.
- P. Malhotra, T. Jiao, D. L. Henann, R. J. Clifton, and P. R. Guduru. Dynamic shearing resistance of hydroxyl-terminated polybutadiene (htpb). *Journal of Applied Physics*, 129(24):245901, 2021. doi: 10.1063/5.0054654.
- L. G. Malito, J. V. Sov, B. Gludovatz, R. O. Ritchie, and L. A. Pruitt. Fracture toughness of ultra-high molecular weight polyethylene: A basis for defining the crack-initiation toughness in polymers. *Journal of the Mechanics and Physics of Solids*, 122:435–449, 2019. ISSN 0022-5096. doi: <https://doi.org/10.1016/j.jmps.2018.09.022>.
- Y. Mao and L. Anand. Fracture of elastomeric materials by crosslink failure. *Journal of Applied Mechanics*, 85(8), 06 2018a. ISSN 0021-8936. doi: 10.1115/1.4040100. 081008.
- Y. Mao and L. Anand. A theory for fracture of polymeric gels. *Journal of the Mechanics and Physics of Solids*, 115:30–53, 2018b. ISSN 0022-5096. doi: <https://doi.org/10.1016/j.jmps.2018.02.008>.
- Y. Mao, B. Talamini, and L. Anand. Rupture of polymers by chain scission. *Extreme Mechanics Letters*, 13:17–24, 2017. ISSN 2352-4316. doi: <https://doi.org/10.1016/j.eml.2017.01.003>.
- T. Matsuda, R. Kawakami, T. Nakajima, and J. P. Gong. Crack tip field of a double-network gel: Visualization of covalent bond scission through mechanoradical polymerization. *Macromolecules*, 53(20):8787–8795, 2020. doi: 10.1021/acs.macromol.0c01485.

- K. Mayumi, J. Guo, T. Narita, C. Y. Hui, and C. Creton. Fracture of dual crosslink gels with permanent and transient crosslinks. *Extreme Mechanics Letters*, 6:52–59, 2016. ISSN 2352-4316. doi: <https://doi.org/10.1016/j.eml.2015.12.002>.
- C. Miehe and L.-M. Schänzel. Phase field modeling of fracture in rubbery polymers. part i: Finite elasticity coupled with brittle failure. *Journal of the Mechanics and Physics of Solids*, 65:93–113, 2014. ISSN 0022-5096. doi: <https://doi.org/10.1016/j.jmps.2013.06.007>.
- C. Miehe, M. Hofacker, and F. Welschinger. A phase field model for rate-independent crack propagation: Robust algorithmic implementation based on operator splits. *Computer Methods in Applied Mechanics and Engineering*, 199(45):2765–2778, 2010a. ISSN 0045-7825. doi: <https://doi.org/10.1016/j.cma.2010.04.011>.
- C. Miehe, F. Welschinger, and M. Hofacker. Thermodynamically consistent phase-field models of fracture: Variational principles and multi-field fe implementations. *International Journal for Numerical Methods in Engineering*, 83(10):1273–1311, 2010b. doi: <https://doi.org/10.1002/nme.2861>.
- I. Miranda, A. Souza, P. Sousa, J. Ribeiro, E. M. S. Castanheira, R. Lima, and G. Minas. Properties and applications of pdms for biomedical engineering: A review. *Journal of Functional Biomaterials*, 13(1), 2022. ISSN 2079-4983. doi: 10.3390/jfb13010002.
- M. Montanari, R. Brighenti, M. Terzano, and A. Spagnoli. Puncturing of soft tissues: experimental and fracture mechanics-based study. *Soft Matter*, 19:3629–3639, 2023. doi: 10.1039/D3SM00011G.
- K. Myronidis, M. Thielke, M. Kopeć, M. Meo, and F. Pinto. Polyborosiloxane-based, dynamic shear stiffening multilayer coating for the protection of composite laminates under low velocity impact. *Composites Science and Technology*, 222:109395, 2022. ISSN 0266-3538. doi: <https://doi.org/10.1016/j.compscitech.2022.109395>.
- S. Narayan and L. Anand. A gradient-damage theory for fracture of quasi-brittle materials. *Journal of the Mechanics and Physics of Solids*, 129:119–146, 2019. ISSN 0022-5096. doi: <https://doi.org/10.1016/j.jmps.2019.05.001>.
- S. Narayan and L. Anand. Fracture of amorphous polymers: A gradient-damage theory. *Journal of the Mechanics and Physics of Solids*, 146:104164, 2021. ISSN 0022-5096. doi: <https://doi.org/10.1016/j.jmps.2020.104164>.

- K. Narumi, F. Qin, S. Liu, H.-Y. Cheng, J. Gu, Y. Kawahara, M. Islam, and L. Yao. Self-healing ui: Mechanically and electrically self-healing materials for sensing and actuation interfaces. In *Proceedings of the 32nd Annual ACM Symposium on User Interface Software and Technology*, UIST '19, page 293–306, New York, NY, USA, 2019. Association for Computing Machinery. ISBN 9781450368162. doi: <https://doi.org/10.1145/3332165.3347901>.
- S. Niu and V. Srivastava. Simulation trained CNN for accurate embedded crack length, location, and orientation prediction from ultrasound measurements. *International Journal of Solids and Structures*, 242:111521, 2022a. doi: <https://doi.org/10.1016/j.ijsolstr.2022.111521>.
- S. Niu and V. Srivastava. Ultrasound classification of interacting flaws using finite element simulations and convolutional neural network. *Engineering with Computers*, 38(5):4653–4662, Oct 2022b. ISSN 1435-5663. doi: 10.1007/s00366-022-01681-y.
- S. Niu, E. Zhang, Y. Bazilevs, and V. Srivastava. Modeling finite-strain plasticity using physics-informed neural network and assessment of the network performance. *Journal of the Mechanics and Physics of Solids*, 172:105177, 2023. ISSN 0022-5096. doi: <https://doi.org/10.1016/j.jmps.2022.105177>.
- L. Nunes. Mechanical characterization of hyperelastic polydimethylsiloxane by simple shear test. *Materials Science and Engineering: A*, 528(3):1799–1804, 2011. ISSN 0921-5093. doi: <https://doi.org/10.1016/j.msea.2010.11.025>.
- Y. Qi, Z. Zou, J. Xiao, and R. Long. Mapping the nonlinear crack tip deformation field in soft elastomer with a particle tracking method. *Journal of the Mechanics and Physics of Solids*, 125:326–346, 2019. ISSN 0022-5096. doi: <https://doi.org/10.1016/j.jmps.2018.12.018>.
- Y. Qi, X. Li, S. P. Venkata, X. Yang, T. L. Sun, C.-Y. Hui, J. P. Gong, and R. Long. Mapping deformation and dissipation during fracture of soft viscoelastic solid. *Journal of the Mechanics and Physics of Solids*, 186:105595, 2024. ISSN 0022-5096. doi: <https://doi.org/10.1016/j.jmps.2024.105595>.
- A. Raina and C. Miehe. A phase-field model for fracture in biological tissues. *Biomechanics and Modeling in Mechanobiology*, 15(3):479–496, Jun 2016. ISSN 1617-7940. doi: 10.1007/s10237-015-0702-0.
- B. D. Reddy. The role of dissipation and defect energy in variational formulations of problems in strain-gradient plasticity. part 1: polycrystalline plasticity. *Continuum*

- Mechanics and Thermodynamics*, 23(6):527–549, Nov 2011. ISSN 1432-0959. doi: 10.1007/s00161-011-0194-9.
- A. J. Rosakis and G. Ravichandran. Dynamic failure mechanics. *International Journal of Solids and Structures*, 37(1):331–348, 2000. ISSN 0020-7683. doi: [https://doi.org/10.1016/S0020-7683\(99\)00097-9](https://doi.org/10.1016/S0020-7683(99)00097-9).
- D. Roylance. Stress-strain curves. *Massachusetts Institute of Technology study, Cambridge*, 2001.
- T. Shen and F. J. Vernerey. Rate-dependent fracture of transient networks. *Journal of the Mechanics and Physics of Solids*, 143:104028, 2020. ISSN 0022-5096. doi: <https://doi.org/10.1016/j.jmps.2020.104028>.
- T. Shen, Z. Song, S. Cai, and F. J. Vernerey. Nonsteady fracture of transient networks: The case of vitrimer. *Proceedings of the National Academy of Sciences*, 118(29):e2105974118, 2021. doi: 10.1073/pnas.2105974118.
- A. Shrivastava, S. M., and N. Gundiah. Crack propagation and arrests in gelatin hydrogels are linked to tip curvatures. *Soft Matter*, 19:6911–6919, 2023. doi: 10.1039/D3SM00637A.
- A. Shukla, G. Ravichandran, and Y. D. Rajapakse. Springer, New York, 2010. ISBN 978-1-4419-0445-4. doi: <https://doi.org/10.1007/978-1-4419-0446-1>.
- S. Shukla, J. Favata, V. Srivastava, S. Shahbazmohamadi, A. Tripathi, and A. Shukla. Effect of polymer and ion concentration on mechanical and drug release behavior of gellan hydrogels using factorial design. *Journal of Polymer Science*, 58(10):1365–1379, 2020. doi: <https://doi.org/10.1002/pol.20190205>.
- J. Sloopman, C. J. Yeh, P. Millereau, J. Comtet, and C. Creton. A molecular interpretation of the toughness of multiple network elastomers at high temperature. *Proceedings of the National Academy of Sciences*, 119(13):e2116127119, 2022. doi: 10.1073/pnas.2116127119.
- H. Somarathna, S. Raman, D. Mohotti, A. Mutalib, and K. Badri. Rate dependent tensile behavior of polyurethane under varying strain rates. *Construction and Building Materials*, 254:119203, 2020. ISSN 0950-0618. doi: <https://doi.org/10.1016/j.conbuildmat.2020.119203>.
- Z. Song, T. Shen, F. J. Vernerey, and S. Cai. Force-dependent bond dissociation explains the rate-dependent fracture of vitrimers. *Soft Matter*, 17:6669–6674, 2021. doi: 10.1039/D1SM00518A.

- V. Srivastava, A. Shukla, and V. Parameswaran. Experimental evaluation of the dynamic shear strength of adhesive-bonded lap joints. *Journal of Testing and Evaluation - J TEST EVAL*, 28, 11 2000. doi: <https://doi.org/10.1520/jte12134j>.
- V. Srivastava, V. Parameswaran, A. Shukla, and D. Morgan. *Effect of Loading Rate and Geometry Variation on the Dynamic Shear Strength of Adhesive Lap Joints*, pages 769–780. Springer Netherlands, Dordrecht, 2002. ISBN 978-0-306-48410-0. doi: https://doi.org/10.1007/0-306-48410-2_71.
- V. Srivastava, S. A. Chester, N. M. Ames, and L. Anand. A thermo-mechanically-coupled large-deformation theory for amorphous polymers in a temperature range which spans their glass transition. *International Journal of Plasticity*, 26(8):1138–1182, 2010a. ISSN 0749-6419. doi: <https://doi.org/10.1016/j.ijplas.2010.01.004>. Special Issue In Honor of Lallit Anand.
- V. Srivastava, S. A. Chester, and L. Anand. Thermally actuated shape-memory polymers: Experiments, theory, and numerical simulations. *Journal of the Mechanics and Physics of Solids*, 58(8):1100–1124, 2010b. ISSN 0022-5096. doi: <https://doi.org/10.1016/j.jmps.2010.04.004>.
- V. Srivastava, J. Buitrago, and S. T. Slocum. Stress analysis of a cryogenic corrugated pipe. In *Proceedings of the ASME 2011 30th International Conference on Ocean, Offshore and Arctic Engineering: Volume 3*, pages 411–422. American Society of Mechanical Engineers, 2011. doi: <https://doi.org/10.1115/OMAE2011-49852>.
- D. Steck, J. Qu, S. B. Kordmahale, D. Tscharnuter, A. Muliana, and J. Kameoka. Mechanical responses of ecoflex silicone rubber: Compressible and incompressible behaviors. *Journal of Applied Polymer Science*, 136(5):47025, 2019. doi: <https://doi.org/10.1002/app.47025>.
- B. Talamini, Y. Mao, and L. Anand. Progressive damage and rupture in polymers. *Journal of the Mechanics and Physics of Solids*, 111:434–457, 2018. ISSN 0022-5096. doi: <https://doi.org/10.1016/j.jmps.2017.11.013>.
- F. Tang, C. Dong, Z. Yang, Y. Kang, X. Huang, M. Li, Y. Chen, W. Cao, C. Huang, Y. Guo, and Y. Wei. Protective performance and dynamic behavior of composite body armor with shear stiffening gel as buffer material under ballistic impact. *Composites Science and Technology*, 218:109190, 2022. ISSN 0266-3538. doi: <https://doi.org/10.1016/j.compscitech.2021.109190>.

- M. Tang, W. Wang, D. Xu, and Z. Wang. Synthesis of structure-controlled polyborosiloxanes and investigation on their viscoelastic response to molecular mass of polydimethylsiloxane triggered by both chemical and physical interactions. *Industrial & Engineering Chemistry Research*, 55(49):12582–12589, 2016. doi: <https://doi.org/10.1021/acs.iecr.6b03823>.
- H. Tu, P. Xu, Z. Yang, F. Tang, C. Dong, Y. Chen, W. Cao, C. Huang, Y. Guo, and Y. Wei. Effect of shear thickening gel on microstructure and impact resistance of ethylene–vinyl acetate foam. *Composite Structures*, 311:116811, 2023. ISSN 0263-8223. doi: <https://doi.org/10.1016/j.compstruct.2023.116811>.
- K. Vaishakh, N. Parambil, and V. Srivastava. Hygroscopic damage of fiber–matrix interface in unidirectional composites: A computational approach. *International Journal of Mechanical Sciences*, 279:109460, 2024. ISSN 0020-7403. doi: <https://doi.org/10.1016/j.ijmecsci.2024.109460>.
- S. P. Venkata, K. Cui, J. Guo, A. T. Zehnder, J. P. Gong, and C.-Y. Hui. Constitutive modeling of bond breaking and healing kinetics of physical polyampholyte (pa) gel. *Extreme Mechanics Letters*, 43:101184, 2021. ISSN 2352-4316. doi: <https://doi.org/10.1016/j.eml.2021.101184>.
- F. Vogel, S. Göktepe, P. Steinmann, and E. Kuhl. Modeling and simulation of viscous electroactive polymers. *European Journal of Mechanics / A Solids*, 48(Complete):112–128, 2014. ISSN 09977538. doi: [10.1016/j.euromechsol.2014.02.001](https://doi.org/10.1016/j.euromechsol.2014.02.001).
- T. Wang, X. Ye, Z. Liu, X. Liu, D. Chu, and Z. Zhuang. A phase-field model of thermoelastic coupled brittle fracture with explicit time integration. *Computational Mechanics*, 65(5):1305–1321, May 2020. ISSN 1432-0924. doi: [10.1007/s00466-020-01820-6](https://doi.org/10.1007/s00466-020-01820-6).
- W. Wang, Y. Zhang, and W. Liu. Bioinspired fabrication of high strength hydrogels from non-covalent interactions. *Progress in Polymer Science*, 71:1–25, 2017. ISSN 0079-6700. doi: <https://doi.org/10.1016/j.progpolymsci.2017.04.001>. Topical Volume on Polymeric Biomaterials.
- Y. Wang, L. Ding, C. Zhao, S. Wang, S. Xuan, H. Jiang, and X. Gong. A novel magnetorheological shear-stiffening elastomer with self-healing ability. *Composites Science and Technology*, 168:303–311, 2018. ISSN 0266-3538. doi: <https://doi.org/10.1016/j.compscitech.2018.10.019>.
- J. Wu, C. McAuliffe, H. Waisman, and G. Deodatis. Stochastic analysis of polymer composites rupture at large deformations modeled by a phase field method. *Computer Meth-*

- ods in Applied Mechanics and Engineering*, 312:596–634, 2016. ISSN 0045-7825. doi: <https://doi.org/10.1016/j.cma.2016.06.010>. Phase Field Approaches to Fracture.
- H. Yang, T. Henzel, E. M. Stewart, and M. Guo. An interpenetrating-network theory of the cytoskeletal networks in living cells. *Journal of the Mechanics and Physics of Solids*, 189:105688, 2024. ISSN 0022-5096. doi: <https://doi.org/10.1016/j.jmps.2024.105688>.
- T. Yin, T. Wu, J. Liu, S. Qu, and W. Yang. Essential work of fracture of soft elastomers. *Journal of the Mechanics and Physics of Solids*, 156:104616, 2021. ISSN 0022-5096. doi: <https://doi.org/10.1016/j.jmps.2021.104616>.
- S. Yuan, T. Tong, Z. Liu, and P. Yang. Explicit double-phase-field formulation and implementation for bending behavior of uhpc-nc composite beams. *Journal of Building Engineering*, 57:104802, 2022. ISSN 2352-7102. doi: <https://doi.org/10.1016/j.jobbe.2022.104802>.
- H. Yuk, T. Zhang, S. Lin, G. A. Parada, and X. Zhao. Tough bonding of hydrogels to diverse non-porous surfaces. *Nature Materials*, 15(2):190–196, Feb 2016. ISSN 1476-4660. doi: <https://doi.org/10.1038/nmat4463>.
- H. Yuk, S. Lin, C. Ma, M. Takaffoli, N. X. Fang, and X. Zhao. Hydraulic hydrogel actuators and robots optically and sonically camouflaged in water. *Nature Communications*, 8(1):14230, Feb 2017. ISSN 2041-1723. doi: <https://doi.org/10.1038/ncomms14230>.
- H. Yuk, C. E. Varela, C. S. Nabzdyk, X. Mao, R. F. Padera, E. T. Roche, and X. Zhao. Dry double-sided tape for adhesion of wet tissues and devices. *Nature*, 575(7781):169–174, Nov 2019. ISSN 1476-4687. doi: [10.1038/s41586-019-1710-5](https://doi.org/10.1038/s41586-019-1710-5).
- P. Zhang, S. Tan, X. Hu, W. Yao, and X. Zhuang. A double-phase field model for multiple failures in composites. *Composite Structures*, 293:115730, 2022. ISSN 0263-8223. doi: <https://doi.org/10.1016/j.compstruct.2022.115730>.
- C. Zhao, X. Gong, S. Wang, W. Jiang, and S. Xuan. Shear stiffening gels for intelligent anti-impact applications. *Cell Reports Physical Science*, 1(12):100266, 2020a. ISSN 2666-3864. doi: <https://doi.org/10.1016/j.xcrp.2020.100266>.
- C. Zhao, Y. Wang, M. Ni, X. He, S. Xuan, and X. Gong. Dynamic behavior of impact hardening elastomer: A flexible projectile material with unique rate-dependent performance. *Composites Part A: Applied Science and Manufacturing*, 143:106285, 2021. ISSN 1359-835X. doi: <https://doi.org/10.1016/j.compositesa.2021.106285>.

- J. Zhao, L. Debertrand, T. Narita, and C. Creton. Fracture of dual crosslink gels with permanent and transient crosslinks: Effect of the relaxation time of the transient crosslinks. *Journal of Rheology*, 66(6):1255–1266, 11 2022. ISSN 0148-6055. doi: 10.1122/8.0000460.
- P.-C. Zhao, W. Li, W. Huang, and C.-H. Li. A self-healing polymer with fast elastic recovery upon stretching. *Molecules*, 25(3), 2020b. ISSN 1420-3049. doi: 10.3390/molecules25030597.
- D. Zheng, S. Lin, J. Ni, and X. Zhao. Fracture and fatigue of entangled and unentangled polymer networks. *Extreme Mechanics Letters*, 51:101608, 2022. ISSN 2352-4316. doi: <https://doi.org/10.1016/j.eml.2022.101608>.
- J. Zhong and V. Srivastava. A higher-order morphoelastic beam model for tubes and filaments subjected to biological growth. *International Journal of Solids and Structures*, 233:111235, 12 2021. ISSN 00207683. doi: <https://doi.org/10.1016/j.ijsolstr.2021.111235>.
- X.-K. Zhu and J. A. Joyce. Review of fracture toughness (g, k, j, ctod, ctoa) testing and standardization. *Engineering Fracture Mechanics*, 85:1–46, 2012. ISSN 0013-7944. doi: <https://doi.org/10.1016/j.engfracmech.2012.02.001>.
- H. Zong, Z. Liu, R. Wei, B. Dong, X. Yang, and W. Zhai. Shear thickening and impact resistance properties of stg in flexible protection application. *Journal of Physics: Conference Series*, 1855(1):012022, mar 2021. doi: <https://dx.doi.org/10.1088/1742-6596/1855/1/012022>.